



HAL
open science

Baroclinic, Kelvin and inertia-gravity waves in the barostrat instability experiment

C Rodda, I D Borcia, P. Le Gal, M Vincze, U. Harlander

► **To cite this version:**

C Rodda, I D Borcia, P. Le Gal, M Vincze, U. Harlander. Baroclinic, Kelvin and inertia-gravity waves in the barostrat instability experiment. *Geophysical and Astrophysical Fluid Dynamics*, 2018. hal-01784584

HAL Id: hal-01784584

<https://hal.science/hal-01784584v1>

Submitted on 3 May 2018

HAL is a multi-disciplinary open access archive for the deposit and dissemination of scientific research documents, whether they are published or not. The documents may come from teaching and research institutions in France or abroad, or from public or private research centers.

L'archive ouverte pluridisciplinaire **HAL**, est destinée au dépôt et à la diffusion de documents scientifiques de niveau recherche, publiés ou non, émanant des établissements d'enseignement et de recherche français ou étrangers, des laboratoires publics ou privés.

1 ***Baroclinic, Kelvin and inertia-gravity waves in the barostat instability***
2 ***experiment***

3 C. Rodda^{†*}, I.D. Borcia[‡], P. Le Gal[‡], M. Vincze[§] & U. Harlander[†]

4 [†]Department of Aerodynamics and Fluid Mechanics, Brandenburg University of Technology (BTU)
5 Cottbus-Senftenberg, Siemens-Halske-Ring 14, D-03046 Cottbus, Germany

6 [‡]Aix Marseille Univ, CNRS, Centrale Marseille, IRPHE, 49 rue F. Joliot-Curie, F-13384, Marseille,
7 France

8 [§]MTA-ELTE Theoretical Physics Research Group, Pázmány P. s. 1/A, H-1117 Budapest, Hungary

9 (*v4.4 released October 2012*)

10 The differentially heated rotating annulus is a laboratory experiment historically designed for modelling
11 large-scale features of the mid-latitude atmosphere. In the present study, we investigate a modified version
12 of the classic baroclinic experiment in which a juxtaposition of convective and motionless stratified layers
13 is created by introducing a vertical salt stratification. The thermal convective motions are suppressed in a
14 central region at mid-depth of the rotating tank, therefore double-diffusive convection rolls can develop only
15 in thin layers located at top and bottom, where the salt stratification is weakest. For high enough rotation
16 rates, the baroclinic instability destabilises the flow in the top and the bottom shallow convective layers,
17 generating cyclonic and anticyclonic eddies separated by the stable stratified layer.

18 Thanks to this alternation of layers resembling the convective and radiative layers of stars, the planetary's
19 atmospheric troposphere and stratosphere or turbulent layers at the sea surface above stratified waters,
20 this new laboratory setup is of interest for both astrophysics and geophysical sciences. More specifically, it
21 allows to study the exchange of momentum and energy between the layers, primarily by the propagation of
22 internal gravity waves (IGW).

23 PIV velocity maps are used to describe the wavy flow pattern at different heights. Using a co-rotating laser
24 and camera, the wave field is well resolved and different wave types can be found: baroclinic waves, Kelvin,
25 and Poincaré type waves. The signature of small-scale IGW can also be observed attached to the baroclinic
26 jet. The baroclinic waves occur at the thin convectively active layer at the surface and the bottom of the
27 tank, though decoupled they show different manifestation of nonlinear interactions. The inertial Kelvin and
28 Poincaré waves seem to be mechanically forced. The small-scale wave trains attached to the meandering jet
29 point to an imbalance of the large-scale flow. For the first time, the simultaneous occurrence of different
30 wave types is reported in detail for a differentially heated rotating annulus experiment.

31 **Keywords:** Baroclinic instability; differentially heated rotating annulus; waves in rotating and stratified
32 fluids; inertia-gravity waves;

33 **1. Introduction**

34 Convective flows driven by temperature gradient are ubiquitous in geophysical and in astro-
35 physical systems. In a large variety of settings, ranging from salinity stratified water basins
36 (Boehrer 2012) to regions of planetary and stellar interiors (Medrano *et al.* 2014) the direction
37 of the temperature gradient is not co-aligned with that of the local gravity. Then the inter-
38 play between stabilising density stratification and the destabilising thermal stratification can
39 yield the emergence of double-diffusive convective instability (Chen *et al.* 1971). The cases
40 where the initial temperature contrast has a perpendicular component to the gravity vector
41 are particularly interesting for mid-scale ocean dynamics (Shibley *et al.* 2017). If planetary
42 (or stellar) rotation is also taken into account, the complexity of the phenomena further in-
43 creases and leads to nontrivial interactions between rotational and convective instabilities. In

*Corresponding author. Email: rodde@b-tu.de

44 the present study, we focus on a rotating double diffusive system in a conceptual laboratory
45 set-up that has been surprisingly rarely investigated in the literature.

46 A plethora of experimental works exists dealing with purely thermally-driven rotating flows
47 (where the density of the fluid parcels is solely determined by their temperature) utilising
48 lateral heating and cooling since the 1950s. The widely studied thermally driven rotating
49 annulus, introduced by Hide (1958), Fultz *et al.* (1959), is a classic laboratory experiment
50 designed to understand the manner in which the atmospheric circulation transports heat
51 from equatorial to polar latitudes. The setup of this experiment consists of a tank with three
52 concentric cylinders filled with pure water. The innermost cylinder (representing the polar
53 region) is cooled, whereas the outer ring (representing the equator) is heated and the tank is
54 mounted on a turntable, so it rotates around its own vertical axis of symmetry. Therefore,
55 the working fluid in the annular cavity is subject to a radial temperature difference and a
56 Coriolis deflection. The combined effect leads, for high enough values of the rotation rate,
57 to the baroclinic instability with the formation of cyclonic and anticyclonic eddies covering
58 the full water column. The baroclinic instability is at the heart of the mesoscale motions
59 in the atmosphere and ocean and gives rise in particular to atmospheric weather systems
60 (Vallis 2006). Besides the baroclinic waves, varying either the magnitude of the temperature
61 difference or the rotation rate, other flow regimes can develop in the annular gap. The four
62 possible regimes are axisymmetric flow, steady waves, vacillation, and irregular flow.

63
64 Many theoretical (Lindzen *et al.* 1982), numerical (Ohlsen and Hart 1989, Randria-
65 mampianina *et al.* 2006), and experimental (Buzyna *et al.* 1989, Von Larcher and Egbers
66 2005, Harlander *et al.* 2011) studies have focused on the so-called amplitude vacillations,
67 i.e., the periodic fluctuations in the intensity of the aforementioned baroclinic eddies, the
68 associated temperature patterns and sought a fundamental understanding of the manner
69 in which these vacillations arise, which are the processes leading to them and how they
70 equilibrate by interacting with the mean flow. The findings of these studies suggest that am-
71 plitude vacillations mainly occur because of nonlinear wave-wave interactions and wave-mean
72 flow interaction but also feedback mechanisms between the fluid interior and the boundary
73 layers (Früh 2014). A special case of a flow which appears like a modulated amplitude
74 vacillation (also known as interference vacillation) is the superposition of two waves with the
75 same horizontal wavenumber, non-orthogonal vertical structures, and different phase speeds
76 (Lindzen *et al.* 1982, Vincze *et al.* 2014).

77
78 In addition to the baroclinic waves, inertial Kelvin modes are known to be resonantly
79 excited in a rotating cylinder in various situations as an elliptic instability (Lacaze *et al.*
80 2004), precessional instability (Lagrange *et al.* 2011, Triana *et al.* 2012), and parametric
81 forcing. The name Kelvin waves here refers to inertial waves modified by stratification
82 having a specific vertical structure and these are not to be confused with coastal Kelvin
83 waves, which are shallow water boundary trapped waves. Guimbard *et al.* (2010) have
84 theoretically investigated the inertial Kelvin modes in a rotating cylinder and the behaviour
85 of the dispersion relation when vertical salinity stratification is introduced. The occurrence
86 of different waves and their interactions can lead to instabilities. For example, the resonance
87 between Rossby and inertial Kelvin waves induces the Rossby-Kelvin instability, which
88 has been studied numerically in the two-layer shallow water model by Gula *et al.* (2009)
89 and experimentally in a rotating annulus for a two miscible fluid layers by Flór *et al.*
90 (2011). **In systems with fluid interfaces, as the latter cited ones, other instabilities such as**
91 **Kelvin-Helmholtz and Hölmböe can arise. These two instabilities, in particular, have been**
92 **found to be a source for the emission of small-scale waves in rotating annulus experiments**
93 **and their occurrence is related to the interface thickness, density, and shear, as discussed by**
94 **Scolan *et al.* (2014).**

95

96 In the present work, we propose a thermohaline version of the differentially heated rotating
 97 annulus, the ‘barostrat’ experiment introduced by Vincze *et al.* (2016), where a continuously
 98 stratified salinity profile is prepared in the annulus cavity before the experiment is run with
 99 the so-called double-bucket technique (Oster and Yamamoto 1963). This particular configura-
 100 tion is not only interesting for investigating the wave regimes that develop in the fluid depth
 101 as well as studying inertial Kelvin/baroclinic wave coupling and the coexistence of different
 102 baroclinic waves, but also to investigate the occurrence of small-scale waves and in particular
 103 inertia gravity waves spontaneously emitted by the baroclinic wave. Recently, several numeri-
 104 cal models (Jacoby *et al.* 2011, Borchert *et al.* 2014, Randriamampianina and del Arco 2015)
 105 and laboratory experiments (Lovegrove *et al.* 2000, Williams *et al.* 2005) have used different
 106 configurations of the rotating annulus experiment to investigate the interaction between large-
 107 scale ‘balanced’ flow components (quasi-geostrophic baroclinic waves) and ‘fast’, small-scale,
 108 ageostrophic inertia-gravity waves.

109 The advantage of the laboratory set up used in this paper in contrast to the classical config-
 110 uration is that, by introducing vertical salinity gradient to the set up, the frequency ratios
 111 between the Brunt-Väisälä (or buoyancy) frequency $N = \sqrt{-g/\rho_0 d\rho/dz}$ – where ρ_0 is a refer-
 112 ence density – and the Coriolis frequency $f = 2\Omega$, where Ω is the angular velocity of the
 113 rotation, rises from $N/f < 1$ (classical set up) to $N/f \simeq 10$ (barostrat). Because the ratio is
 114 larger than unity, IGW propagation is expected to be qualitatively similar to the atmospheric
 115 case, as it follows from the dispersion relation:

$$\omega^2 = \frac{N^2(k^2 + l^2) + f^2 n^2}{k^2 + l^2 + n^2} = N^2 \cos^2(\gamma) + f^2 \sin^2(\gamma), \quad (1)$$

116 where the intrinsic frequency in the rotating frame of reference ω of the wave is determined by
 117 the buoyancy frequency N , the Coriolis frequency f , and $\gamma = \arctan(n/\sqrt{k^2 + l^2})$, the angle
 118 between the phase velocity and the horizontal plane, set by horizontal wavenumbers k , l and
 119 vertical wavenumber n . Due to the finite domain of values of the sine and cosine functions in
 120 (1), IGWs can only exist for specific frequencies ω . More specifically, in Figure 2(b), which
 121 represents the buoyancy frequency profile $N(z)$ as calculated from the measured density profile
 122 in panel (a), the two distinct existence regions, according to the values of f and N , are shown.
 123 At the top and the bottom of the tank (green regions) $N < f$ and therefore $N < \omega < f$, while
 124 in the region in the middle (light blue) $f < N$ and so, in this case, $f < \omega < N$.
 125 The criterion for baroclinic instability reads (Hide and Mason 1975):

$$Bu = \left(\frac{N D}{f L} \right)^2 < 0.581, \quad (2)$$

126 and we see that for large N/f the aspect ratio D/L needs to be small to find baroclinic
 127 instability. In the thermohaline annulus, this is automatically fulfilled since the convective
 128 layers are thin and hence D has to be replaced by the thickness λ of the convective layers.

129

130 The paper is organised as follows: in section 2 we briefly introduce the most important
 131 features of the experiment set up and the measurement techniques used, in section 3 we
 132 described the data analysis methods applied to our measurements. Section 4 first focuses on
 133 the large scale wave regimes and interactions occurring at different fluid heights in our tank
 134 and then investigates inertia-gravity waves along the jet of the baroclinic waves. Summary
 135 and conclusions are given in section 5.

136 2. Experimental set-up and data acquisition

137 The experiments considered in this paper were performed at the BTU Cottbus-Senftenberg
 138 laboratories using the same apparatus introduced in previous work by Vincze *et al.* (2016).
 139 For a detailed description of the experimental set up, we refer the reader to their paper. In
 140 this section, we will only report the most significant parameters.

141 2.1. Experimental set-up

142 The annular tank consists of an inner cylinder, cooled by a thermostat, and an outer cylinder,
 143 heated by a heated coil, with radii equal to $a = 4.5$ cm and $b = 12$ cm respectively. The
 144 annular cavity of width $L = b - a = 7.5$ cm has a flat bottom, a free surface, and was filled
 145 up to the height $D = 10.5$ cm. The lateral temperature difference ΔT was set to 10 K, after
 146 this value was reached in the experiment, the rotation rate of the turntable about the vertical
 147 axis was slowly increased ($\Delta\Omega = 0.1$ rpm every 2 minutes) until the final value $\Omega = 4$ rpm. A
 148 sketch of experimental set-up with the double diffusive convection developing in the barostat
 149 experiment is shown in Figure 1.

150 Applying the standard two-bucket technique (Oster and Yamamoto 1963) a salinity profile
 151 was created in the annular gap. The prepared stable vertical salinity profiles have been
 152 measured with a conductivity meter at the beginning of the experiment, before starting
 153 the rotation and at the end of the experiment, after stopping the rotation. Successively
 154 the conductivity has been converted to density. The calculated vertical density profiles are
 155 plotted in Figure 2(a), from which we can distinguish three layers in the tank: two shallow
 156 layers (whose thickness, indicated by the grey shading, is approximatively two centimeters)
 157 on the top and the bottom of the tank, both characterised by constant density, and a middle
 158 layer with an almost linear density profile. The distinct interfaces separating the regions,
 159 visible in the plot, correspond to the frontier of the convective layers. The plot of the time
 160 averaged azimuthal velocities for the four measured heights (Figure 2(c)) shows that the
 161 zonal flow is prograde at the surface ($z = 94$ mm), then retrograde at $z = 75$ mm, almost
 162 zero in the middle motionless stratified layer ($z = 47$ mm), and again prograde at the lowest
 163 measured height ($z = 21$ mm). The plots for the density, the buoyancy frequency N , and the
 164 azimuthal velocity (Figure 2) are in excellent agreement with the ones shown by Vincze *et al.*
 165 (2016) for similar experimental settings. The boundary conditions of no-flux for salinity at
 166 the surface and the bottom of the water column imposes a zero concentration gradient at
 167 these boundaries even before a temperature gradient is applied. In this configuration, only
 168 the two separate shallow fluid layers can be baroclinically destabilised. Indeed, the vertical
 169 salt stratification opposes the thermal convective motions until the ratio of the (horizontal)
 170 thermal density difference and the (vertical) salinity-induced density difference exceeds a
 171 certain critical threshold. Then double-diffusive convection rolls develop in thin layers located
 172 in regions where the salt stratification is weakest. An important clarification is needed:
 173 the curves plotted in Figure 2 for the density and the buoyancy frequency N are obtained
 174 measuring the temperature compensated conductivity, so they depend only on the variations
 175 of the salinity content in the water column. However, density variations depend both on
 176 the salinity (δS) and the temperature (δT) variations in the form $\delta\rho/\rho_0 = -\alpha\delta T + \beta\delta S$,
 177 where α is the thermal expansion coefficient and β is the haline contraction coefficient.
 178 Although we do not have measurements of the thermal gradients and thus no access to
 179 the Brunt-Väisälä frequency associated to the temperature stratification, we know that
 180 temperature vertical gradients only exists in the convective cells at the top and bottom
 181 of the water column, whereas in the bulk (i.e., outside the top and bottom cells) the
 182 thermal contribution to N is zero. In the convective cells, convection and the baroclinic
 183 instability mix the temperature field and consequently decreases the vertical difference

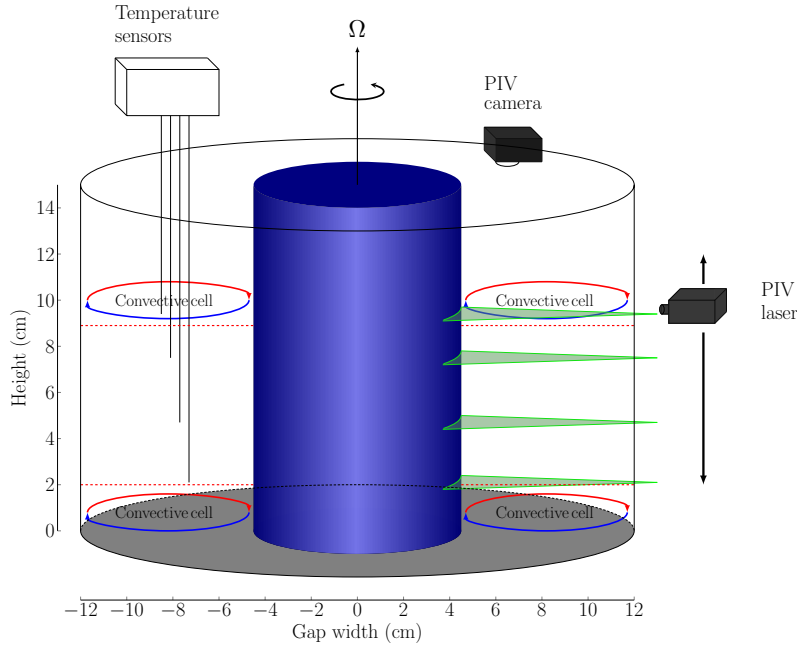


Figure 1. Sketch of the double-diffusive convection in the barostrat experiment and of the experimental set-up with PIV levels and temperature sensors positions. The red dashed lines indicate the interfaces between the convective regions and the calm region at the heights $z_{top} = 8.9$ cm and $z_{bottom} = 2$ cm.

184 of temperature in these layers. For this reason, we speculate that in the upper/lower
 185 mixed layer the value of N is rather low. Using the numerical simulations of Borchert *et al.*
 186 (2014) and specially their Figure 3c, the value for N should be constraint in the range 0.08 to 0.4
 187

188 For our thermohaline experimental setup, it is useful to introduce a local version of the
 189 Taylor and thermal Rossby numbers:

$$Ta(z) = \frac{4\Omega^2 L^5}{\nu^2 \lambda(z)}, \quad (3)$$

190

$$Ro_T(z) = \frac{\lambda(z) g \alpha \Delta T}{\Omega^2 L^2}, \quad (4)$$

191 where Ω is the rotation rate, ΔT is the horizontal difference of temperature, L is the gap width,
 192 D is the total fluid depth, ν is the kinematic viscosity, g is the acceleration of gravity, and
 193 α the volumetric thermal expansion coefficient (whose value varies according to temperature,
 194 salinity, and pressure). These two nondimensional numbers, generally used to study the flow
 195 regime in the differentially heated rotating annulus, are now depending on the vertical extent
 196 of a convective cell at height z , $\lambda(z)$, which is determined by the initial buoyancy frequency
 197 profile $N(z)$ and the lateral temperature contrast ΔT . Note that, because the flow states
 198 depend not only on the lateral temperature difference and on the rotation rate but also on
 199 the convective cell thickness, different flow states may be observed at different heights. The
 200 condition that the initial saline density difference between the top and bottom of the cell
 201 cannot outreach the horizontal thermal density difference between the cylindrical walls define
 202 the thickness of the cell $\lambda(z)$, which can, therefore, be calculated using Chen's formula:

$$\lambda(z) = \frac{g \alpha \Delta T}{N^2(z)}. \quad (5)$$

203 For increasing N , λ decreases until it reaches a critical value, λ_{crit} , below which viscous effects
 204 hinder the formation of convective cells (as reported by Chen *et al.* (1971)). Vincze *et al.*

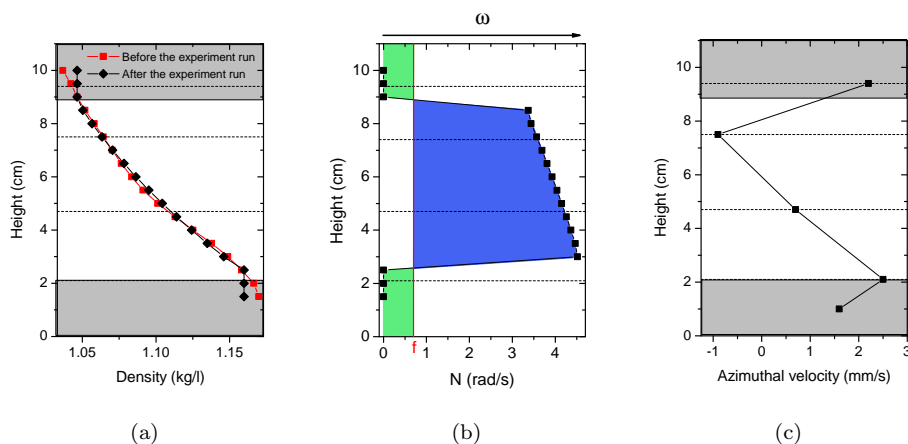


Figure 2. Vertical density (a) buoyancy frequency (b) and azimuthal velocity (c) profiles. The dashed lines correspond to the PIV measurement heights, the grey shaded areas indicate the convective layers at the top and the bottom of the tank. (a) the density is measured before starting rotation (red line) and after stopping the rotation (black line). (b) buoyancy frequency calculated from the density measured after the rotation. The vertical red line shows the value of the Coriolis frequency $f = 2\Omega$, the two green areas indicate the frequencies interval in which IGWs can be found ($N < \omega < f$) for the regions where the salinity stratification is weak. The central light blue area indicates the frequencies interval in which IGWs can be found ($f < \omega < N$) for the region with strong salinity stratification. In the latter case, IGWs are expected to propagate similarly to the ones in the atmosphere. (c) plot of the azimuthal velocities averaged over time for the four measured heights. It can be noticed that the zonal flows is prograde at the surface, then retrograde at $z = 75$ mm, corresponding to the convective region, almost zero in the middle motionless stratified layer, and again prograde at the lowest z .

205 (2016) found that the formation of two separate convective layers followed the Chen relation
 206 and the layers at the top and the bottom were observed to be around 2 cm thick.

207 **2.2. PIV and temperature data acquisition**

208 To investigate the flow regimes at different water heights (indicated by the dashed lines in
 209 Figure 2 and by the green laser planes in Figure 1), a co-rotating particle image velocimetry
 210 (PIV) system is mounted on the cylindrical annulus. A camera (GoPro Hero 4, screen
 211 resolution 1920×1080 , fps = 30) together with a green laser (Laser Linos Nano 250-532-100,
 212 wavelength $\lambda = 532$ nm, maximum power 300 mW) are fixed on a vertical bar mounted at
 213 the outer cylinder. The laser produces a continuous horizontal light plane of 1 mm thickness
 214 which illuminates tracer particles (a mixture of hollow glass and silver coated hollow glass
 215 spheres with diameter range distribution $2 - 20 \mu\text{m}$ and mean density $\rho = 1.1 \text{ g/cm}^3$) in
 216 the fluid. Applying the Stokes' law, the settling velocity at which the particles move towards
 217 the middle region of the tank ranges between $V_t = 0.05 - 4.7$ cm per hour. The particles are
 218 added to the fluid when the density profile is prepared at the beginning of the experiment.
 219 Considering that the experiment runs for maximum 6 hours, at least the smallest particles
 220 are expected to be found 1.5 cm below the surface and above the bottom of the tank at the
 221 end of it. In addition to the settling velocity, we have to take into account that the convective
 222 motions at the top and the bottom of the tank are mixing the PIV particles rather effectively.
 223 Therefore, at the measurement heights the particles remain in neutral buoyancy during the
 224 measurement time $\simeq 12$ minutes.

225 The field of view recorded by the co-rotating camera, fixed at close range to the water surface,
 226 covers approximatively one third of the annulus and allows to gain close-ups of the velocity
 227 fields, giving a better resolution in particular on the small-scale features. The recorded videos,
 228 having each a total duration of 12 minutes, are processed with the free Matlab toolbox
 229 UVmat (see <http://servforge.legi.grenoble-inp.fr/projects/soft-uvmat>) and the horizontal
 230 components of the velocities are obtained. The percentage of velocity vectors excluded during

231 the PIV analysis and then interpolated is less than 1.5%. The *rms* difference between the CIV
 232 (Correlation Image Velocimetry) and the smoothed velocity field is $rms = 0.5 - 0.6$ pixels
 233 for a typical displacement of 5 pixels. This gives an estimation of the PIV error 10% – 12%,
 234 comparable with the a posteriori error estimation (see Appendix A for more details).

235

236 In addition to the PIV system, five temperature sensors have been placed at the same levels
 237 for which we also do the PIV measurements, i.e., 94 mm, 75 mm, 47 mm, and 21 mm. The
 238 sensors are placed in the center of the annulus gap and diametrically opposite to the side
 239 where we do the PIV measurements. Hence the sensors, having a diameter of 500 μm and a
 240 Reynolds number of the order $Re = 1$, do not affect the PIV measurements. The temperature
 241 sensors have a sampling rate $\Delta t = 1$ s and are able to record the data for the entire duration
 242 of the experiment (about 2 hours). Thanks to the temperature sensors, we have long time
 243 measurements simultaneously at all the chosen fluid heights. A schematic drawing of the
 244 experimental set up with the temperature sensors and the PIV apparatus is given in Figure
 245 1.

246 3. Data analysis methods

247 In this section we describe the two statistical methods, i.e., harmonic analysis and empirical
 248 orthogonal functions, we use to analyse our velocity fields. In particular, we are interested in
 249 studying whether the baroclinic dynamics are different in the two unstable layers.

250 The harmonic analysis is a form of signal demodulation in which the user specifies the
 251 frequencies to be examined and applies least square techniques to solve for the constituents,
 252 (for an extensive description of the method we refer to the textbook of Thomson and Emery
 253 (2001)). This method is very useful to investigate the spatial patterns associated with a
 254 single given frequency and in particular we use it to emphasise the waves modes at different
 255 heights. Moreover, it has the advantage to be very robust even for short time series.

256 Besides harmonic analysis, we apply the empirical orthogonal function (EOF) analysis to the
 257 PIV data (a complete description of the method can be found in the textbook of Navarra
 258 and Simoncini (2010)). Without specifying particular frequencies in advance this method
 259 provides a description of the spatial patterns of variability of the data series and their
 260 temporal variation, breaking the data into orthogonal functions or ‘modes of variability’ and
 261 thus is widely used in geosciences (e.g., Lorenz 1956). One mode of variability can detect
 262 more than one frequency and therefore can comprise a more complex dynamics such as
 263 interactions between waves. The advantage of using both methods independently is that
 264 we can investigate time dependent patterns (with the EOF analysis, whereas the harmonic
 265 analysis gives only the spatial patterns) and give them a physical interpretation by comparing
 266 the results obtained with the two techniques. Indeed, while the interpretation of the spatial
 267 patterns obtained by the harmonic analysis is clear, connecting the EOFs to the physical
 268 modes is not trivial.

269

270 The emission of inertia-gravity wave packets from the baroclinic jet is a phenomenon
 271 highly localised in space and time (Viúdez and Dritschel 2006). Therefore, it is very diffi-
 272 cult to capture these small-scale waves using the two statistical methods described in this
 273 section. A quantity often used as an indicator for IGWs is the horizontal velocity divergence
 274 $\nabla_{\mathbf{h}} \cdot \mathbf{u} = \partial u / \partial x + \partial v / \partial y$ (O’Sullivan and Dunkerton 1995, Borchert *et al.* 2014). The horizontal
 275 divergence contains a balanced part, as defined by quasi-geostrophic balance, and an imbal-
 276 anced part that is related to IGWs. We use the horizontal divergence to study the small-scale
 277 waves, their behaviour in time, their wavenumbers and frequencies. The last ones are obtained
 278 by computing two dimensional fast Fourier transforms.

279 3.1. Harmonic analysis

280 We consider the velocity field V , measured by PIV at an arbitrary grid point in our measured
281 domain $V(t_n)$. This quantity can be expressed by a Fourier expansion

$$V(t_n) = \bar{V} + \sum_{q=1}^M [A_q \cos(\omega_q t_n) + B_q \sin(\omega_q t_n)] + V_r(t_n) \quad (6)$$

282 with $q = 0, 1, \dots, M$ and M is the number of distinct frequencies to be analysed, \bar{V} is the
283 temporal mean, V_r the residual of the time series (it could contain other kinds of components),
284 $t_n = n\Delta t$ the time, ω_q a constant frequency, A_q and B_q are the harmonic coefficients of the
285 Fourier series. The amplitude of the frequency component q is

$$C_q = (A_q^2 + B_q^2)^{1/2}, \quad (7)$$

286 and the phase is

$$\phi_q = \tan^{-1}(B_q/A_q) \quad (8)$$

287 The M distinct frequencies to be analysed are chosen as the main peaks in the horizontal
288 velocity spectra at each measured fluid height. The horizontal velocity components, measured
289 along one radial line taken in the middle of the camera field of view, are selected. The
290 frequency spectrum for each of these points is then calculated by using a fast Fourier
291 transform algorithm and then the spectrum is averaged for the points of this particular
292 chosen line.

293

294 A truncated Fourier series is thereafter fitted to the time series containing the frequencies
295 to be analysed, ω_q . The variance e^2 is computed for each point

$$e^2 = \left\{ V(t) - \left[\bar{V} + \sum_{q=1}^M [A_q \cos(\omega_q t) + B_q \sin(\omega_q t)] \right] \right\}^2 \quad (9)$$

296 where $V(t)$ are the measured PIV velocities, \bar{V} is the temporal mean and A_q , B_q are the
297 Fourier coefficients of the harmonics obtained by a least-square fit.

298 We estimate the amplitudes, C_q , and phases, ϕ_q , of the various components by minimising
299 the variance. Once the amplitudes and the phase for a certain frequency are calculated, the
300 corresponding velocity field can be plot on the domain recorded by the camera (approximately
301 one third of the tank). For rather steady waves, we can graphically reconstruct the entire
302 annulus using symmetric properties. The reconstructed plots are made by combining together
303 3 or 4 partial plots obtained from the harmonic analysis. These are shifted by a phase $\phi = 120^\circ$,
304 when 3 images are used or $\phi = 90^\circ$ when 4 images are used. The figures have then been
305 combined together (with some overlapping) to reconstruct the full annulus, relying on the
306 hypothesis of patterns regular in space.

307 3.2. Empirical orthogonal functions

308 To analyse data that contain oscillations in time or in space and time as a propagating signal,
309 it is useful to use a modified version of the standard EOF analysis, the so called complex
310 empirical orthogonal functions (CEOFs) (Pfeffer *et al.* 1990).

311 For a harmonic wave of the form $V(\mathbf{x}, t) = \text{Re}[U(\mathbf{x}) \exp(-i\omega t)]$ a peculiar phase relation
312 that indicates propagation is a quarter wavelength shift. CEOF analysis enhances this phase
313 relation changing the available data by adding a new data set obtained by shifting all data by
314 one quarter wavelength by using a Hilbert transform (Navarra and Simoncini 2010). Therefore,

315 a single CEOF represents a single mode split into two patterns with a phase difference of $\pi/2$
 316 (the real and imaginary part of the CEOF).

317 To calculate the CEOFs we follow the same approach described in Harlander *et al.* (2011),
 318 considering the CEOFs method for a simultaneous analysis of more than one field. Such a
 319 coupled analysis is useful in our case where one field is the u - and the other is the v -component
 320 of the velocity. We proceed in the following way to find coupled propagating patterns: complex
 321 time series of the velocity components are formed from the original time series and their Hilbert
 322 transforms:

$$323 \quad u_c(\mathbf{x}, t) = u(\mathbf{x}, t) + iu_H(\mathbf{x}, t), \quad (10)$$

$$324 \quad v_c(\mathbf{x}, t) = v(\mathbf{x}, t) + iv_H(\mathbf{x}, t), \quad (11)$$

324 where $u(\mathbf{x}, t)$, $v(\mathbf{x}, t)$ are the time series of the horizontal components of the velocity mea-
 325 sured by PIV at each location in the recorded domain, $u_H(\mathbf{x}, t)$ and $v_H(\mathbf{x}, t)$ are the Hilbert
 326 transforms of $u(\mathbf{x}, t)$, $v(\mathbf{x}, t)$ and i is the imaginary unit.

327 The Hilbert transform of the original time series X_t with Fourier decomposition

$$328 \quad X_t = \sum_{\omega} \zeta(\omega) \exp(-2\pi i\omega t), \quad (12)$$

328 is defined as:

$$329 \quad X_t^H = \sum_{\omega} \zeta^H(\omega) \exp(-2\pi i\omega t), \quad (13)$$

329 where $\zeta^H(\omega) = i\zeta(\omega)$ for $\omega \leq 0$ and $\zeta^H(\omega) = -i\zeta(\omega)$ for $\omega > 0$. For the computation of the
 330 Hilbert transforms, we used the algorithm described by Marple (1999).

331 Thereafter, we form extended time series by combining the $v_c(\mathbf{x}, t)$ time series with the $u_c(\mathbf{x}, t)$
 332 time series and rewriting them as a row-vector in the form of $\mathbf{U} = (u_1, \dots, u_M, v_1, \dots, v_M)$. The
 333 data matrix D is written in the form of

$$334 \quad D = \begin{pmatrix} U_1(t_0) & U_2(t_0) & \dots & U_M(t_0) \\ U_1(t_1) & U_2(t_1) & \dots & U_M(t_1) \\ \vdots & \vdots & & \vdots \\ U_1(t_N) & U_2(t_N) & \dots & U_M(t_N) \end{pmatrix} \quad (14)$$

334 where the rows represent the state vector at the spatial grid points $U(t_n) = (U_1(t_n), \dots, U_M(t_n))$
 335 at time t_n and the columns represent the time series $U_m(t) = (U_m(t_0), \dots, U_m(t_N))^T$ at the spatial
 336 point m .

337 From the data matrix, we calculate the covariance matrix

$$338 \quad F = D^T D, \quad (15)$$

338 The CEOFs are the eigenvectors of F and the so called Principal Components (PCs) are
 339 the corresponding time-dependent coefficients.

340

341 4. Results

342 4.1. Propagating waves at different fluid heights

343 A puzzling result from the experiments done by Vincze *et al.* (2016) was that baroclinic waves
 344 have been found only in the upper convective layer (see Figure 1). The reason for this might
 345 be damping due to bottom Ekman layer effects. In order to obtain a clear picture of the waves
 346 developing at the different fluid heights in the tank, we first consider frequency spectra of

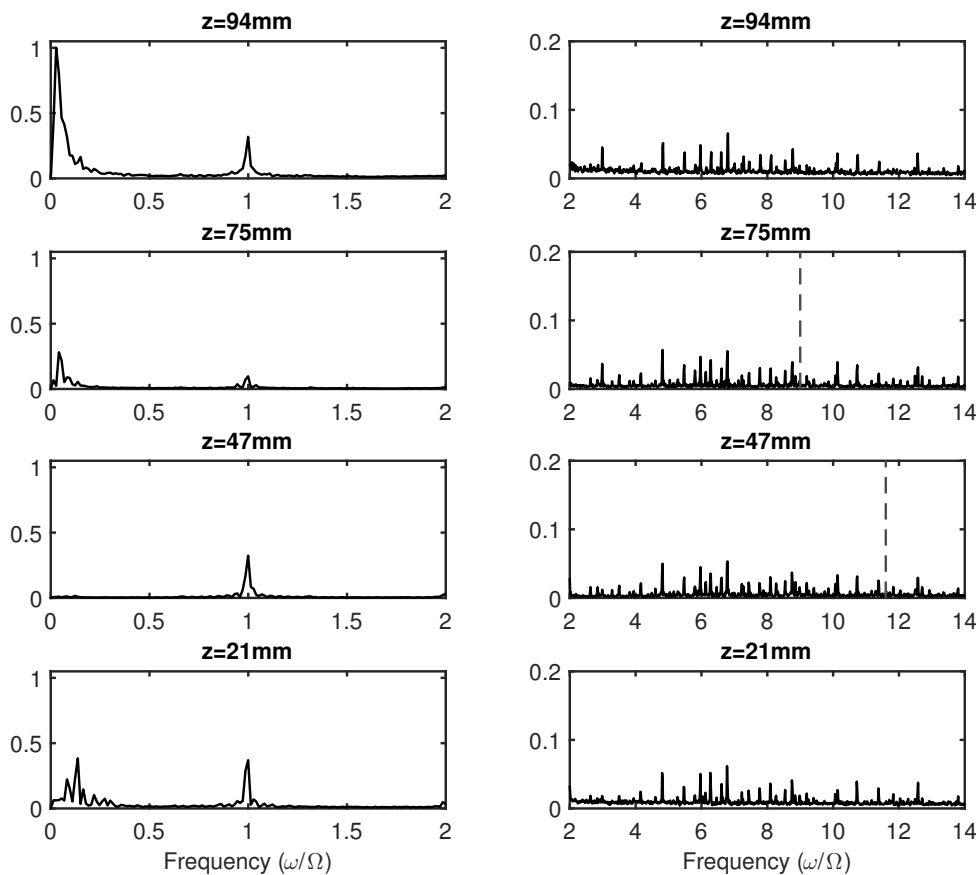


Figure 3. Velocity frequency spectra for the different heights. On the left the low frequencies, $0 < \omega < f$, on the right high frequencies, $f < \omega$. Note that the spectra amplitude on the left plot differs from the one on the right. The vertical dashed line indicates the value of N .

347 the horizontal velocity, obtained as described in Section 3.1, from which we can identify the
 348 dominant frequencies at each height, (i.e., measured from the bottom of the tank: 94 mm, 75
 349 mm, 47 mm, and 21 mm).

350 We have separated the spectra into two windows: $0 < \omega < f$ (Figure 3 left) and $f < \omega$
 351 (Figure 3 right). The grey dashed lines in the figures indicate the value of the buoyancy
 352 frequency N at the measurements heights where known. Peaks for low frequencies appear
 353 in the upper layer, for the frequency $\omega = 0.03\Omega$, at heights $z = 94$ mm (stronger) and
 354 $z = 75$ mm (weaker) and in the bottom layer ($z = 21$ mm), for the frequency $\omega = 0.14\Omega$. In
 355 the middle layer ($z = 47$ mm), instead, there is no peak in the low frequency range. Another
 356 peak, at $\omega = \Omega$, can be seen for all the layers, with a stronger signal at the bottom of the
 357 tank. Finally, in all layers there are peaks at frequencies larger than f .

358 Using the harmonic analysis as described in section 3.1, we can reconstruct the velocity fields
 359 corresponding to the most prominent peaks (Figure 5). The left column shows the baroclinic
 360 waves, one in the uppermost layer ($z = 94$ mm and $z = 75$ mm) close to the surface, and one
 361 in the bottom layer ($z = 21$ mm), with different azimuthal wave numbers, $m = 3$ and $m = 4$
 362 respectively.

363

364 It is instructive now to use the $Ta-Ro_T$ regime diagram to compare the flow regimes observed
 365 for the two baroclinically unstable top and bottom layers with data from the literature for the

366 nonsalt stratified, purely thermal configuration. Once baroclinic instability has set in, for the
 367 experiments where pure water is used, the convective cell covers the whole fluid depth. For
 368 the comparison we consider two separate data set collected at the BTU laboratory using the
 369 same experimental apparatus described in Section 2. The first data set is an investigation of
 370 the flow regimes in a broad range of the Ta - Ro_T parameter space by Von Larcher and Egbers
 371 (2005). We reproduced the regime diagram proposed in their paper in Figure 4, where the
 372 different flow regimes are indicated by the lines and the wavenumbers are given. The second
 373 data set here considered is a study by Vincze *et al.* (2015) which investigate the properties of
 374 the baroclinic instability by considering different initial conditions (i.e., the lateral difference
 375 of temperature was kept constant whilst the rotation rate was increased (spin up condition
 376 \uparrow) or decreased (spin down condition \downarrow Table 1) between each measurement). The four cases
 377 chosen for comparison are plotted (black-diamond shaped marker) in Figure 4 and indicated
 378 by the letters A-D. Our barostrat experiment data for the top and bottom layer are plotted
 379 in red and blue dots respectively. The values of Ta and Ro_T calculated using (4) and (3), the
 380 thickness of the layer (λ) or the total fluid depth, and the observed wavenumbers are listed
 381 in Table 1 for the second data set and the barostrat top and bottom layers.

382 One can clearly see that the thin layers of the thermohaline experiment data are located
 383 in a region where baroclinic waves with $m = 3$ and $m = 4$ have both been observed in the
 384 experiments by Von Larcher and Egbers (2005) and between $m = 3$ and $m = 4$ from the study
 385 by Vincze *et al.* (2015) (note that our initial conditions correspond to the spin up ones).

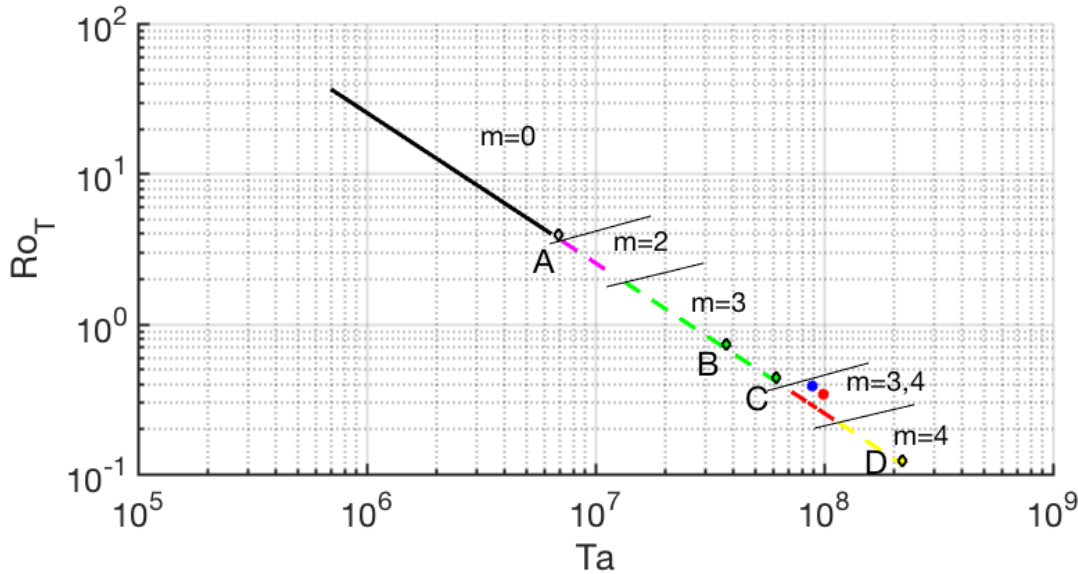


Figure 4. Regime diagram in the Ta - Ro_T space. The flow regime observed in the top and bottom layers in the barostrat experiment are compared with data available from literature for the same experimental setup, but for the purely thermal configuration (see text and Table 1 for more details).

386 As we mentioned before, besides baroclinic waves also other waves can be expected to
 387 rise in our experimental setup. The middle column of Figure 5 shows the velocity pattern
 388 corresponding to the peak at frequency $\omega = \Omega$. We identify this pattern as inertial Kelvin
 389 waves modified by stratification. There are several examples in the literature of inertial Kelvin
 390 mode, also called the spin-over inertial mode, driven by precession either due to the rotation of
 391 the laboratory by the Earth (i.e., in a spherical shell (Triana *et al.* 2012)) or in a precessional
 392 cylinder (i.e., Lagrange *et al.* 2011). Moreover, inertial Kelvin waves might be excited by
 393 elliptical instability, as reported by Lacaze *et al.* (2004). In our case the inertial Kelvin mode
 394 is more likely due to imperfect alignment of the rotation axis with respect to gravity. In a

	λ (cm)	α (10^{-6} K $^{-1}$)	Ro_T	Ta	wavenumber m
Classical setup					
A	13.5	207	3.95	6.88×10^6	0-2
B	13.5	207	0.72	3.75×10^7	3(↑); 4 (↓)
C	13.5	207	0.44	6.20×10^7	3(↑); 4 (↓)
D	13.5	207	0.12	2.21×10^8	4
Barostrat					
Bottom layer barostrat	2	327	0.38	8.87×10^7	4
Top layer barostrat	1.7	297	0.34	9.95×10^7	3

Table 1. Comparison of the wavenumbers and Ro_T and Ta numbers calculated with (4) and (3) for the data from the paper by Vincze *et al.* (2015) and the two baroclinically unstable layers at the top and the bottom of the barostrat experiment. λ is the total fluid depth for the classical setup and the thickness of the convective layer for the barostrat experiment. The values of the thermal expansion coefficient α have been corrected for the salinity and the temperature. The arrows at the side of the wavenumbers mark spin-up \uparrow and spin-down \downarrow initial conditions.

395 system with a free surface this imperfection might force an inertial Kelvin mode even if a true
 396 precession of the rotation axis is absent (personal communication with Patrice Meunier).

397 Due to the fact that our measurements are not simultaneous, we do not have phase information
 398 and hence we cannot investigate in detail the vertical structure of the inertial Kelvin wave
 399 and compare it with the analytical solutions found by Guimbard *et al.* (2010) for a rotating
 400 stratified cylinder. Nevertheless, our experiment shows that the amplitude of the inertial
 401 Kelvin waves varies with depth as can be noticed in Figure 3 and Figure 5 (see colorbar). This
 402 suggests that a structure of the wave along the vertical axis is indeed present. Moreover, it
 403 can be noticed in Figure 5 that at the top ($z = 94$ mm and $z = 75$ mm) and at the bottom
 404 ($z = 21$ mm) of the tank the inertial Kelvin wave has a radial structure that differs from
 405 the middle region ($z = 47$ mm), namely it shows a higher radial wavenumber. This spatial
 406 modulation along the radius might originate from the existence in the top and bottom layers
 407 of the baroclinic instability. Gula *et al.* (2009) and Flór *et al.* (2011) reported instabilities
 408 resulting from resonances between Rossby and inertial Kelvin eigenmodes for a two layer flow
 409 in a rotating annulus. However, no clear signal of such resonance can be observed in our
 410 experiment, in particular since the mean Rossby number is too small and this resonance just
 411 happens for large Ro although some interactions are detected.

412 In the right column of Figure 5 the reconstructed velocity field for one of the main peaks
 413 with frequencies larger than f , for instance $\omega = 6.8\Omega$, is shown. Similar structures can be
 414 found for the other prominent peaks for frequencies $\omega > \Omega$ and are present in all layers. It is
 415 also interesting to notice that most of these peaks appear at the same frequency, not changing
 416 with the height. Obviously, the horizontal structure is similar to the inertial Kelvin wave,
 417 but in this case the amplitude does not decrease in the direction of the outer wall and the
 418 wave propagates prograde. Remarkably, we found very similar high frequency waves in an
 419 experiment carried out with the same set up, but where we only rotate the cylindrical tank
 420 without any lateral temperature difference and vertical salinity stratification. We speculate
 421 that these waves with frequencies $\omega > f$ might be surface wave modes of the Poincaré type.
 422 They might be excited by a weak sloshing at the free surface and, in the case of the barostrat
 423 experiment, also at the interface between the layers of different density. We do not further
 424 investigate these weak gravity wave modes but will focus on the signature of *frontal* gravity
 425 waves that are very localised in space and time. Such localised wave packets move with the
 426 baroclinic jet and Fourier analysis of local time series is hence not a proper tool to detect
 427 those waves. More details on the IGW field related to the baroclinic front shall be given in
 428 Section 4.3 after discussing the baroclinic waves in the next section.

429 4.2. Determination of the baroclinic wave dynamics in the two unstable layers

430 In this section we investigate in more detail the similarities and differences between the
 431 baroclinic waves appearing in the top and bottom layer.

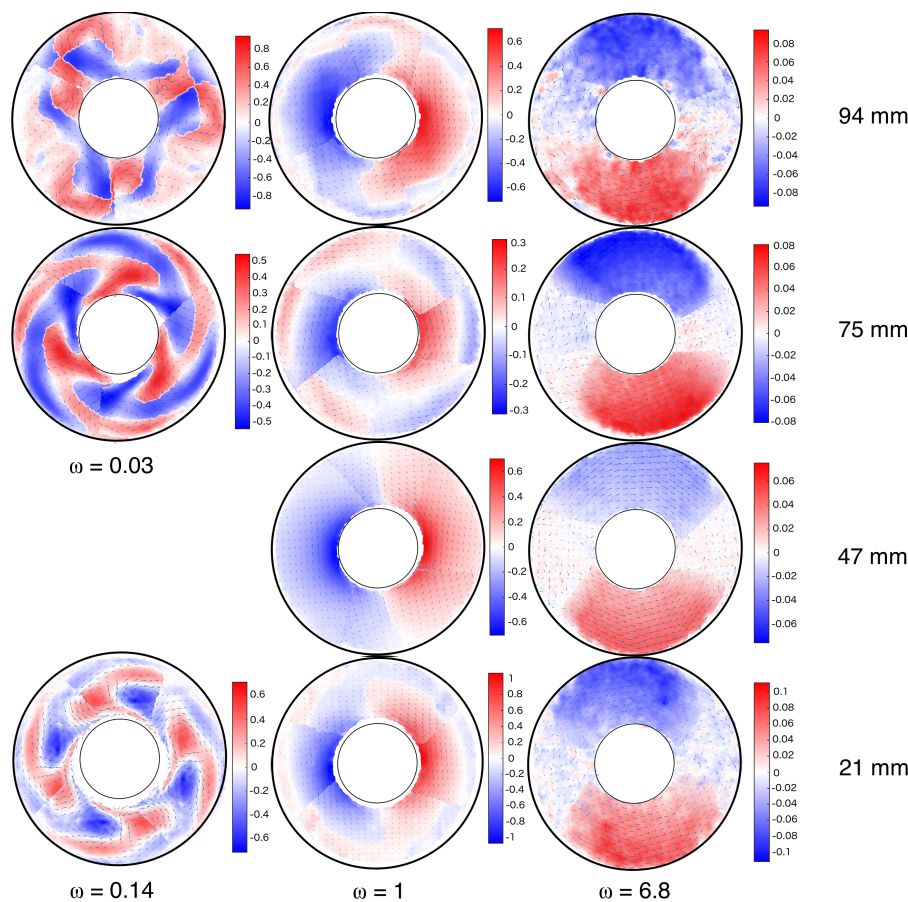


Figure 5. Reconstructed velocity field, using the harmonic analysis, for the principal peaks in the three layers. In the first column on the left are shown the baroclinic waves, $m = 3$ in the uppermost layer (first and second lines from the top) and $m = 4$ for the bottom layer (bottom line in figure). The central columns shows the inertial Kelvin wave, for all layers. In the column on the right is shown the field obtained for the main peak at high frequencies $\omega = 6.8\Omega$. All the frequencies are normalised by Ω .

432 To do so, we performed a CEOF analysis (see section 3.2) of the measured horizontal velocity
 433 field. Figure 6 shows the first ten eigenvalues of the covariance matrix in the uppermost layer
 434 in the tank (Figure 6(a)) and in the bottom layer (Figure 6(b)). Each eigenvalue stands for
 435 the variance that can be explained by the corresponding complex function, the CEOF.

436

437 For the top layer ($z = 94$ mm), the first and the second eigenvalues, explaining together
 438 85% of the total variance, are related to the baroclinic mode and its first harmonic (a power
 439 spectrum of the PCs shows one single peak for each PC at $\omega = 0.04\Omega$ and $\omega = 0.08\Omega$
 440 respectively, these peaks correspond to the ones detected previously by the FFT analysis).
 441 The third eigenvalue, explaining 3.4% of the variance, corresponds to the second harmonic of
 442 the baroclinic wave and the inertial Kelvin wave (two peaks in the PC spectrum at $\omega = 0.12\Omega$
 443 and $\omega = \Omega$). The fourth eigenvalue, explaining 2.6% of the variability, is related to the inertial
 444 Kelvin mode.

445 The eigenvalue spectrum for the bottom layer ($z = 21$ mm) is quite different as can be seen in
 446 Figure 6(b). Also in this case, the first eigenvalue is related to the dominant baroclinic mode,
 447 but it explains only 39% of the total variance and the power spectrum of its correspondent
 448 PC shows a multitude of peaks with frequencies very close to the ones shown in Figure 9(a),
 449 and in addition a peak for $\omega = \Omega$, suggesting a complex dynamics and interactions among
 450 waves. We shall discuss these interactions in more detail in the following text. The second

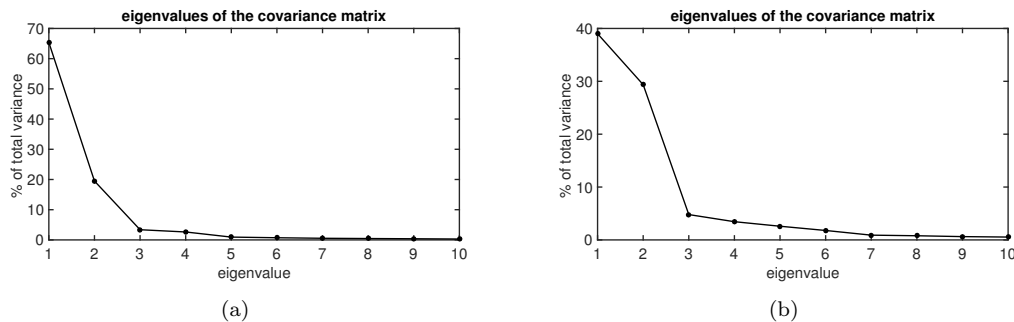


Figure 6. Variance of the first 10 eigenvalues of the coupled u and v velocities for the top layer (a) $z = 94$ mm and the bottom layer (b) $z = 21$ mm.

451 eigenvalue, 29% of the variance, is related to the inertial Kelvin mode interacting with the
 452 baroclinic wave (the PC spectrum shows a peak for $\omega = 0.14\Omega$ and $\omega = \Omega$). The third and the
 453 fourth, explaining 4.8% and 3.4% of the total variance, show a broad spectrum of frequencies
 454 and are not easy to interpret as physical modes. The fifth and sixth eigenvalues, explaining
 455 2.6% and 1.8% of the variability, are related to the second harmonic of the inertial Kelvin
 456 mode $\omega = 2\Omega$. With respect to the eigenvalues of the covariant matrix for the uppermost layer
 457 (Figure 7(a)) we have a significant reduction of the first eigenvalue. Moreover, an interaction
 458 between the baroclinic wave and the inertial Kelvin wave seems to play an important role in
 459 the dynamic of this layer, as both frequencies are contributing to the second CEOF.

460 A similar behaviour, for which the dominant component is smaller by about 20% compared
 461 to the steady wave regime has been observed by Hignett (1985) in case of an amplitude
 462 vacillating regime (AV).

463 If we now consider the first CEOFs for the top layer (Figure 7(c)) and for the bottom layer
 464 (Figure 7(d)) and their respective PCs (Figure 7(a) and 7(b)) we can see that in the top layer
 465 the fluid is in a steady wave regime, where the baroclinic wave shows a regular behaviour and
 466 has a very low phase speed (0.0057 rad/s), while in the bottom layer the baroclinic wave shows
 467 a variation of the amplitude in time with a phase speed of 0.0157 rad/s. Usually a metastable
 468 transient AV has a very high phase speed, circa 5 times faster than the finally equilibrated
 469 flow (Früh and Read 1997). This supports our assumption that the flow in the bottom layer
 470 is in the vacillation regime. For AV the amplitude of the wave varies periodically while the
 471 shape of the wave pattern remains constant. The strength of the vacillation is characterized
 472 by a vacillation index I_v defined over one vacillation cycle as

$$I_v = \frac{A_{max} - A_{min}}{A_{max} + A_{min}}. \quad (16)$$

473

474 Hignett (1985) indicates as critical vacillation index $I_v = 0.05$. This value separates the flow
 475 to be in steady regimes ($I_v < 0.05$) and amplitude vacillation regimes ($I_v > 0.05$). For the
 476 bottom layer of our experiment the value for the vacillation index is $I_v = 0.19$, while for the
 477 top layer $I_v = 0.03$.

478 For a steady wave regime it has been observed in many baroclinic wave experiments
 479 (e.g., Hide *et al.* 1977, Hignett 1985, Früh and Read 1997)) that the amplitude spectrum is
 480 composed almost entirely of the dominant component and its harmonics. This is also the case
 481 for the upper layer of our barostat experiment. The peaks corresponding to the dominant
 482 wavenumber $m = 3$ and its harmonics are dominating the low frequency spectrum plotted
 483 for temperature measurements at $z = 94$ mm in Figure 8(a). In Figure 8 the reconstructed
 484 waves, baroclinic, first and second harmonics with frequencies and wavenumbers $\omega_0^t = 0.04\Omega$,
 485 $m_0^t = 3$, $\omega_1^t = 0.08\Omega$, $m_1^t = 6$, and $\omega_2^t = 0.12\Omega$, $m_2^t = 9$ respectively, are shown. Differently
 486 from what was observed by Hignett (1985) and Hide *et al.* (1977), for which in most of the

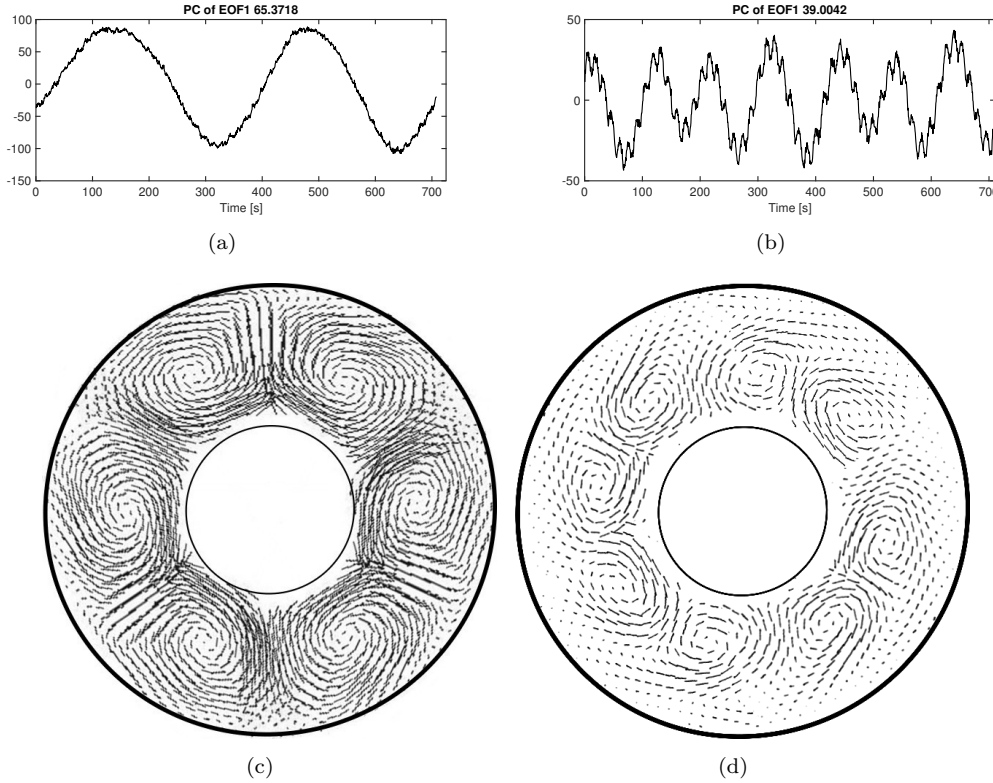


Figure 7. Comparison between the first CEOFs and PCs for the top layer ($z = 94$ mm) and the bottom layer ($z = 21$ mm). (a) PC of the first eigenvalue $z = 94$ mm, (b) PC of the first eigenvalue $z = 21$ mm. (c) Real part of the CEOF of the first eigenvalue at $z = 94$ mm and (d) Real part of the CEOF of the first eigenvalue at $z = 21$ mm

487 experiments the second harmonic was strongly pronounced, in our case the fundamental
 488 wave and the first harmonic are the most energetic ones. Moreover, it has been shown by
 489 Fröh and Read (1997) that for steady waves the harmonic triad shows a more persistent and
 490 pronounced phase locking than the long wave triads.

491

492 Buzyna *et al.* (1989) have represented a particular case of amplitude vacillation regime as
 493 due to an interference of two waves with the same azimuthal wavenumber and different phase
 494 speed. This regime is referred to as interference vacillation. The basis of this approach has
 495 been that a travelling, modulated wave can be represented as a linear superposition of two
 496 waves of the same azimuthal wavenumber, but with different phase speeds or frequencies.
 497 Figure 9(a) shows the spectrum obtained from the temperature sensor at $z = 21$ mm. We
 498 identify two identical shaped baroclinic waves with $m = 4$ at the frequencies $\omega_1^b = 0.089\Omega$
 499 and $\omega_2^b = 0.13\Omega$, indicated in Figure 9(a). Three other peaks with significant variance are
 500 recognisable, one at $2\omega_1^b - \omega_2^b = 0.048\Omega$, at $2\omega_2^b - \omega_1^b = 0.17\Omega$, and at $\omega_1^b + \omega_2^b = 0.22\Omega$. The
 501 first two frequencies indicate the nonlinear interaction of the baroclinic waves ω_1^b and ω_2^b and
 502 the mean zonal flow as reported in detail in Buzyna *et al.* (1989). Figures 9(d), 9(e) show
 503 the velocity fields, obtained with the harmonic analysis, for the frequencies $2\omega_1^b - \omega_2^b$ and
 504 $2\omega_2^b - \omega_1^b$. The spatial pattern of a baroclinic wave $m = 4$ can be seen in both figures, as one
 505 would expect from the wave-mean flow interaction.

506 A second nonlinear interaction can be identified in our experiment: the two baroclinic waves
 507 (ω_1^b and ω_2^b) interact nonlinearly forming a triad $\omega_1^b + \omega_2^b$ that might become resonant. The
 508 reconstructed velocity fields are shown in Figures 9(b), 9(c) and 9(f). As we have seen, the
 509 interaction scenario is more complex than in the case of a steady wave. Moreover, in addition to
 510 the linear interaction between baroclinic waves, also the inertial Kelvin wave seems to interact

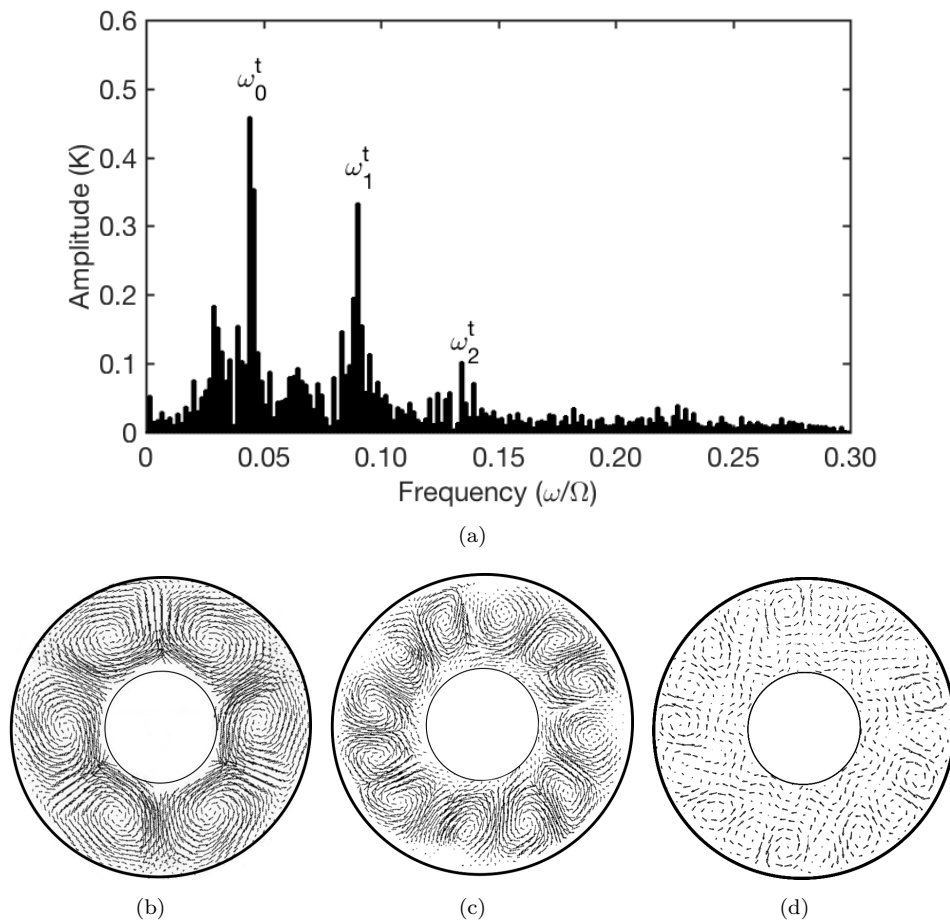


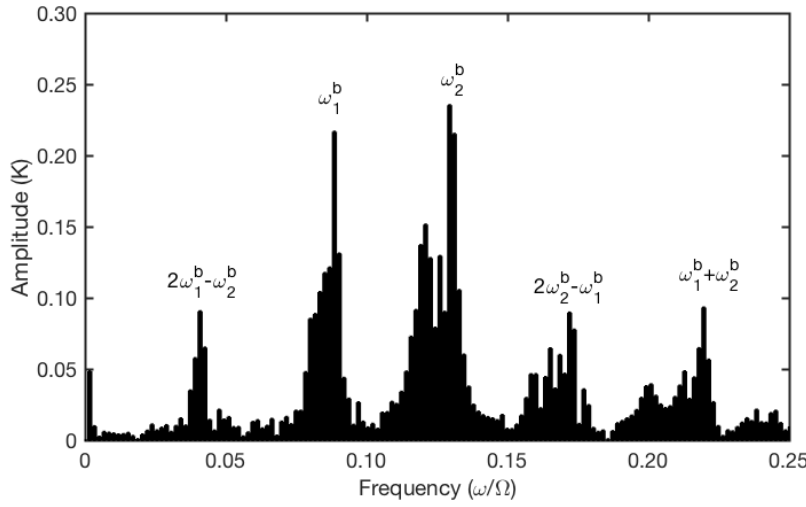
Figure 8. (a) low frequencies spectra from temperature data at $z = 94$ mm. The three peaks correspond to a baroclinic wave and its first and second harmonics: $\omega_0^t = 0.04\Omega$, $\omega_1^t = 0.08\Omega$ and $\omega_2^t = 0.12\Omega$; the velocity fields corresponding to these most energetic modes reconstructed using the CEOF analysis are plotted in (b),(c) and (d) respectively. The three waves of frequencies ω_0^t , ω_1^t and ω_2^t (at $z = 94$ mm) form a harmonic triad with azimuthal wavenumbers $m_0^t = 3$, $m_1^t = 6$, and $m_2^t = 9$.

511 with them, as already discussed. Fröh and Read (1997) also observed a complex interaction
 512 scenario in amplitude vacillation regimes, and found that in this case long wave triads are
 513 usually observed.

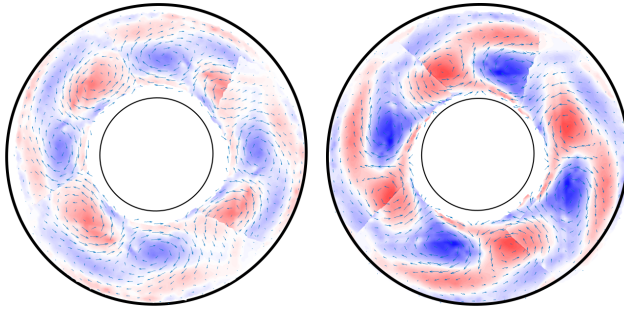
514 It is interesting to notice that interference vacillation has been observed by Harlander *et al.*
 515 (2011) in the classical configuration of the thermally driven annulus. However, in their case
 516 there was no indication that the two waves were coupled through nonlinear interactions but
 517 they appeared to be a linear superposition of two modes of different zonal wave number
 518 drifting at different speeds. In our thermohaline version of the experiment, on the contrary,
 519 the amplitude vacillation results from linear interactions between two waves having the same
 520 wave number leading to a mean zonal flow and nonlinear interactions between the two waves
 521 and the mean zonal flow, more in agreement to the results from Buzyna *et al.* (1989).

522 4.3. Inertia-gravity waves

523 So far we focused on the large-scale modes and their interactions. However, besides the
 524 already discussed baroclinic waves and inertial Kelvin waves, it is instructive to investigate
 525 IGWs occurrence at the baroclinic wave fronts. Such waves are very localised in space and
 526 time. In the paper by Vincze *et al.* (2016) wave trains whose characteristics are compatible

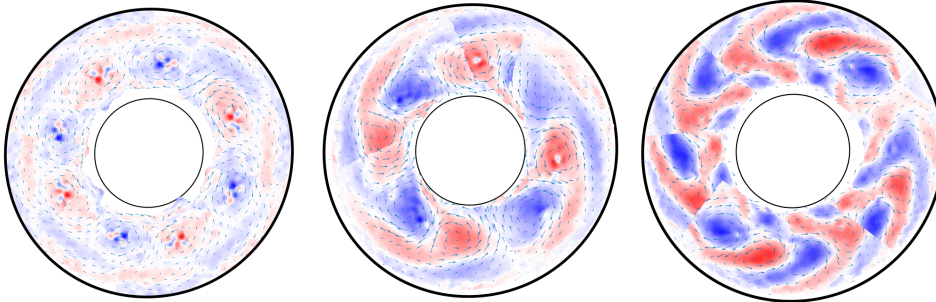


(a)



(b)

(c)



(d)

(e)

(f)

Figure 9. (a) low frequencies spectra from temperature data at $z = 21$ mm. The five peaks (whose velocity fields, reconstructed using the harmonic analysis, are shown in (b)-(f)) correspond respectively to two baroclinic waves ($\omega_1^b = 0.089\Omega$, $\omega_2^b = 0.13\Omega$ and $m = 4$), their nonlinear interactions with the mean flow ($2\omega_1^b - \omega_2^b = 0.048\Omega$, $2\omega_2^b - \omega_1^b = 0.17\Omega$ and $m = 4$), and the nonlinear interaction between the two main waves ($\omega_1^b + \omega_2^b = 0.22\Omega$ and $m = 8$).

527 with IGWs have been detected and a qualitative inspection at the PIV measurements with
 528 numerical simulations of spontaneous emission of IGWs from baroclinic fronts by O'sullivan
 529 and Dunkerton (1995) show a good qualitative agreement.

530

531 4.3.1. Wave trains at $z = 94$ mm

532 We start the discussion on small-scale structures considering the uppermost layer, at
 533 $z = 94$ mm, and in the next subsection we shall present the results obtained for the height

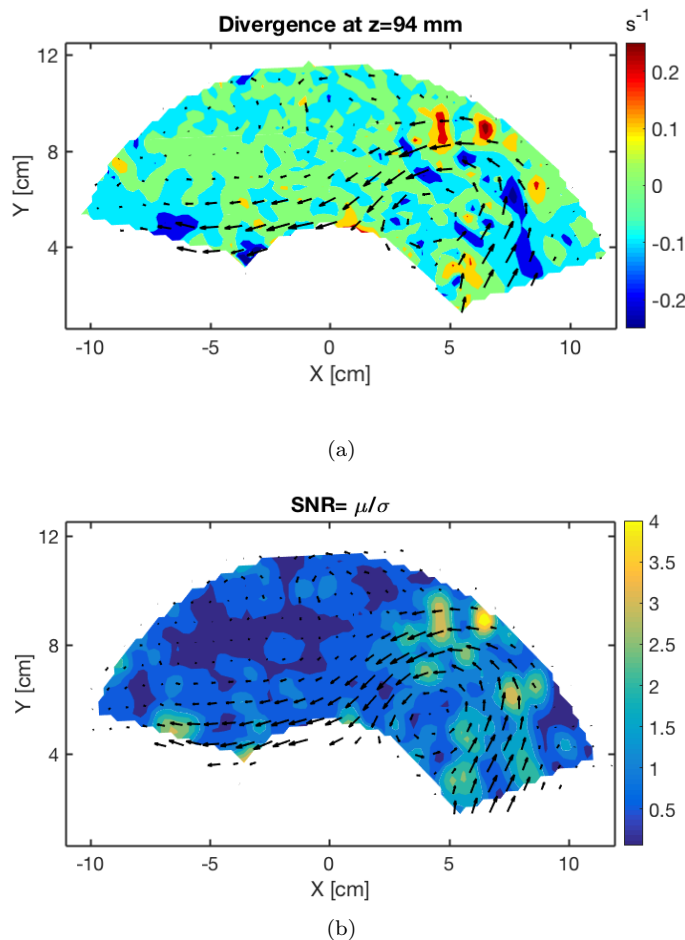


Figure 10. (a) Horizontal divergence at $z = 94$ mm, for $t = 535$ s. The arrows are showing the velocity field while the colour map represents the horizontal divergence. The horizontal wavelengths are: ($\lambda_x = 1$ cm, $\lambda_y = 0.8$ cm). (b) Signal-to-noise ratio, defined as $SNR = \mu/\sigma$. In the region along the jet the signal of small waves can be clearly distinguished from the background noise.

534 $z = 75$ mm. The other measurement heights are not presented because no clear signal of
 535 small-scale wave trains has been found.

536

537 In order to identify possible signals of IGWs, we consider the divergence of the horizontal
 538 velocity field shown in Figure 10(a) for the measurement height $z = 94$ mm. The signal-to-
 539 noise ratio, defined as $SNR = \mu/\sigma$ where σ is the square root of the mean variances of the
 540 background noise and μ is the locally averaged divergence field, spans the range of values 2-4
 541 in the region along the jet where the small-scale waves are visible, indicating that this signal
 542 can be distinguished from the measurement noise (as it can be seen in Figure 10(b)). See
 543 Appendix A for more details about SNR .

544 It can be noticed that for the shown layer most of the divergence signal is associated to the
 545 small-scale waves. Moreover, we can see a wave train structure clearly related to small-scale
 546 phenomena attached to the baroclinic jet. Similar structures are visible in most of our data,
 547 embedded in the baroclinic wave and showing up intermittently.

548

549 It is instructive to further investigate how these small-scale waves travel with respect
 550 to the baroclinic jet. The reason is that observations in the atmosphere by Uccellini and

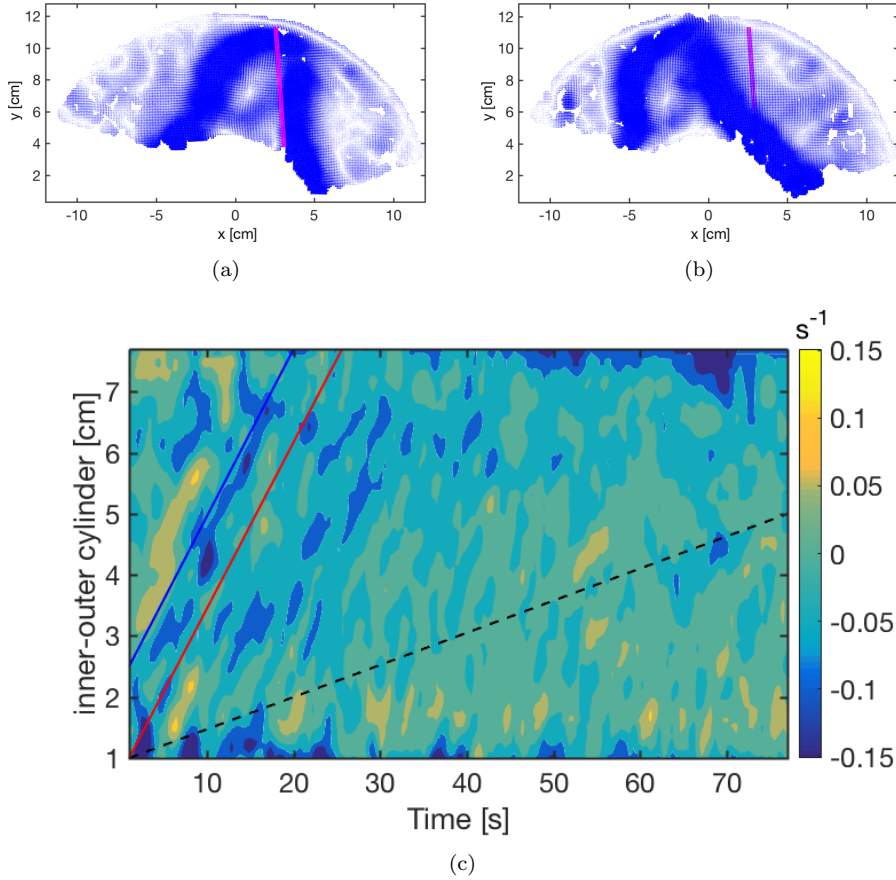


Figure 11. Baroclinic wave jet and position of the line along which the Hovmöller plot is taken (a) at $t_0 = 0$, i.e., the beginning of the Hovmöller plot in (c) and (b) at $t_1 = t_0 + 75$ s, i.e., the end of the Hovmöller plot in (c). (c) Hovmöller plot for the divergence at the entrance of the baroclinic wave at $z = 94$ mm. The dashed line is plotted to show the drift speed of the baroclinic wave, and the red line shows the mean value of the zonal flow in the jet region ($u_0 = 3 \text{ mm s}^{-1}$). The phase velocity of the small-scale waves, measured from this plot and indicated by the blue line is 3 mm s^{-1} , the same as u_0 .

551 Koch (1987) identified intense low frequency IGW in the jet exit regions and hypothesised
 552 spontaneous imbalance as source mechanism. Other observations by Fritts and Nastrom
 553 (1992) have highlighted a conspicuous enhancement of gravity wave activity in the vicinity
 554 of jets and fronts and our experimental study seems to be in line with these numerical and
 555 observational findings. To examine these regions, at $z = 94$ mm, we took two different cuts,
 556 one parallel to the entrance of the baroclinic wave (Figure 11) and one parallel to the exit
 557 of the baroclinic wave (Figure 12). Because we record our data in the system of reference
 558 co-rotating with the tank and the baroclinic wave moves prograde, the wavefront is crossing
 559 our line just for a short time, as it can be seen in Figures 11(a), 11(b), 12(a), and 12(b).
 560 Hence, the most prominent travelling waves can be found in the period $10 \text{ s} < t < 20 \text{ s}$ in
 561 Figure 11(c) and $15 \text{ s} < t < 30 \text{ s}$ in Figure 12(c), when the red line in Figures 11(a), 11(b)
 562 and Figures 12(a), 12(b) is along the entrance and the exit region of the jet respectively.
 563 For a quantitative comparison, we plotted in Figure 11(c) and 12(c) the drift speed of the
 564 baroclinic wave (dashed line) and the mean value of the zonal flow in the jet region (red line).
 565 Remarkably, the phase velocity of the small-scale waves (blue lines) is in both cases similar
 566 to the one of the zonal flow. Compared to the baroclinic wave, the wave packets move faster,
 567 with phase speed equal to 3 mm s^{-1} at the entrance and 5 mm s^{-1} at the exit region of the
 568 baroclinic wave respectively, but are attached to it.

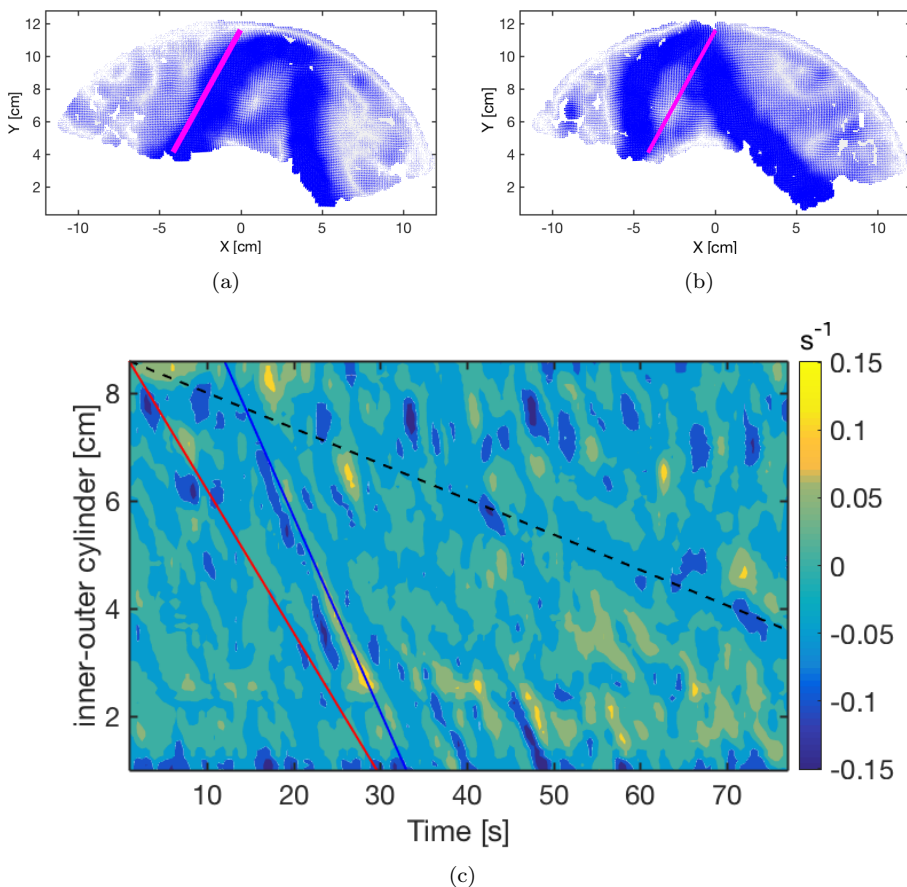


Figure 12. Baroclinic wave jet and position of the line along which the Hovmöller plot is taken (a) at $t_0 = 0$, i.e., the beginning of the Hovmöller plot in (c), and (b) at $t_1 = t_0 + 75$ s, i.e., the end of the Hovmöller plot in (c). (c) Hovmöller plot for the divergence at the exit of the baroclinic wave at $z = 94$ mm. The dashed line is plotted to show the drift speed of the baroclinic wave, and the red line shows the mean value of the zonal flow in the jet region ($u_0 = 3$ mm s^{-1}). The phase velocity of the small-scale waves, measured from this plot and indicated by the blue line is 5 mm s^{-1} .

570 Subsequently, we want to verify whether the intrinsic frequency of the measured small-scale
 571 waves is consistent with IGW dispersion relation. The intrinsic frequency ω_i is the frequency
 572 of a wave relative to the flow, i.e., the wave frequency measured by an observer drifting with
 573 the mean flow:

$$\omega_i = \omega_m - u_0 k, \tag{17}$$

574 ω_m is the frequency measured in the co-rotating system of reference, u_0 is the wind speed and
 575 k the wave vector along the jet.

576 For the uppermost layer ($z = 94$ mm), considering a zonal flow in the jet $u \simeq 3$ mm s^{-1} ,
 577 consistent with the PIV measurement, wavevector $k = 2\pi/\lambda \simeq 3$ cm^{-1} and the measured
 578 frequency $\omega_m = 1/6$ $s^{-1} = 1.04$ rad s^{-1} the obtained intrinsic frequency is $\omega_i \simeq 0.1$ rad s^{-1} .
 579 The finding of a frequency lower than f might seem surprising, however we recall that at this
 580 measurement height the salinity stratification is weak, as we already have shown in the green
 581 areas in Figure 2(b), where we can notice that the value of N due to the salinity at $z = 94$ mm
 582 is zero. **As we previously pointed out, the contribution of temperature stratification to the**
 583 **value of N close to the water surface is not measured experimentally and thus the gradients are**
 584 **difficult to estimate. However, keeping in mind that convection and baroclinic instability imply**
 585 **a strong mixing, added to the fact that heat losses at the surface weaken the temperature**
 586 **gradients in the top layer, it is not unreasonable to consider $N < 0.1$ rad/s and hence the**
 587 **waves inside the IGW frequency range, although we cannot prove it firmly:**

$$|N| < \omega \simeq 0.1 \text{ rad s}^{-1} < 0.836 \text{ rad s}^{-1} = |f|, \quad (18)$$

588 From Figure 11(c) and 12(c) we realised that the wave packet travels with the jet. This is
 589 further in agreement with our finding for the frequency, where $\omega_m = 1.04 \text{ rad s}^{-1} \simeq u_0 k =$
 590 0.94 rad s^{-1} that suggests small-scale waves travelling with the jet.

591 Despite the fact that the waves observed in the experiment are not plane and the dispersion
 592 relation ignores latitudinal and vertical shear, using the intrinsic frequency we can get an
 593 estimation of the vertical wavelength using the dispersion relation solved for λ_z :

$$\lambda_z = \sqrt{\frac{\lambda_x^2 \lambda_y^2 (\omega_i^2 - f^2)}{(\lambda_x^2 + \lambda_y^2) (N^2 - \omega_i^2)}}. \quad (19)$$

594 The estimated vertical wavelength is therefore $\lambda_z^{94} \simeq 5 \text{ cm}$ (for $N = 0$) this order of magnitude
 595 being compatible with the thickness of the convective layer.

596

597 4.3.2. Wave trains at $z = 75 \text{ mm}$

598 We continue the discussion on the small-scale waves signal in this section considering now
 599 the data at the measurement height $z = 75 \text{ mm}$. We recall that this height is in the stratified
 600 region where $N > f$, for this reason IGWs are expected to show similarities with atmospheric
 601 gravity wave packets; the frequencies range for IGWs at this height is highlighted by the light
 602 blue coloured central region in Figure 2(b). Furthermore we want to recall that the baroclinic
 603 wave with $m = 3$ is present at $z = 75 \text{ mm}$ even though it is weaker and drifts in the opposite
 604 direction with respect to the baroclinic wave observed at the height $z = 94 \text{ mm}$ (see Figure
 605 5).

606 We follow the data analysis presented in the previous subsection discussing the analogies
 607 and the differences between the waves observed at the two heights.

608

609 Figure 13 shows the plot of the horizontal divergence (a) in a snapshot at the time $t = 706 \text{ s}$
 610 where a wave train can be seen, similarly to the one found at $z = 94 \text{ mm}$ (Figure 10(a)).
 611 The related signal-to-noise ratio, calculated as described in Appendix A, is plotted in Figure
 612 13(b). The maximum of SNR corresponds to the position of the wave train in the plot above,
 613 pointing to a clear distinction of the signal from the background noise. It can be noticed
 614 that, contrarily to what we observed for $z = 94 \text{ mm}$, at this height the wave train is not
 615 positioned on the baroclinic wave jet, but ahead of the cold front.

616

617

618 Because the baroclinic jet is weaker at this fluid height, and moreover the small-scale waves
 619 are not positioned along it we decided not to repeat the analysis done for $z = 94 \text{ mm}$ where
 620 we have chosen two lines along the entrance and the exit regions of the jet (Figure 11 and 12).

621 Instead, for the $z = 75 \text{ mm}$ level we chose an arc of the circle of radius $r = 8 \text{ cm}$ (see
 622 Figure 14(a)), i.e., at the middle of the gap width, to construct a space-time diagram from
 623 which we derive a frequency-wavenumber diagram. The Hovmöller plot of the divergence
 624 along this arc is shown in Figure 14(b) and the correspondent 2D spectra in Figure 14(c). By
 625 Doppler shifting the dispersion relation using $u_0 = 1 \text{ mm s}^{-1}$ and the horizontal wavenumber
 626 $K_H = 5 \text{ cm}^{-1}$ we obtain the dispersion curves plotted with red, black and yellow dashed
 627 lines in Figure 14(c) for vertical wavelengths $\lambda_z^{75} = 1, 0.3, 0.2 \text{ cm}$ respectively. Obviously, the
 628 curve with $\lambda_z^{75} = 0.2 \text{ cm}$ best fits the plotted data. We hence find that the estimated values
 629 for the vertical wavelengths at the two different fluid heights (by using (19) for $z = 94 \text{ mm}$
 630 and by plotting the dispersion curves for $z = 75 \text{ mm}$) are very different: $\lambda_z^{94} \simeq 5 \text{ cm}$ and
 631 $\lambda_z^{75} \simeq 0.2 \text{ cm}$. This tells us that the upper layer waves have a horizontal phase speed and a

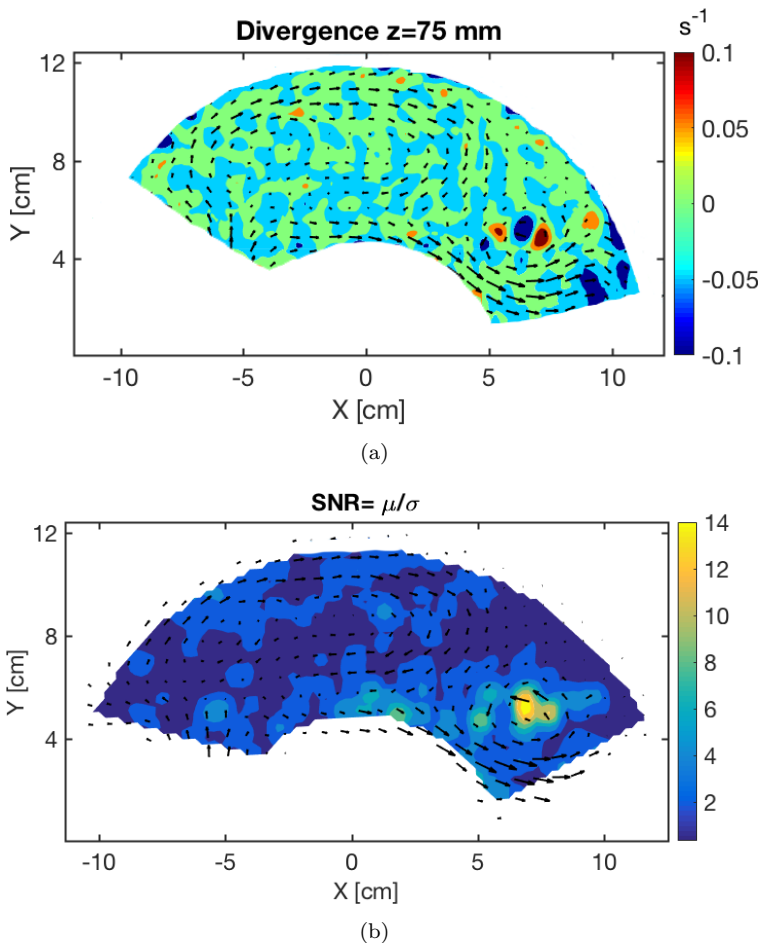


Figure 13. (a) Horizontal divergence at $z = 75$ mm, for $t = 706$ s. The arrows are showing the velocity field while the colour map represents the horizontal divergence. (b) Signal-to-noise ratio, defined as $SNR = \mu/\sigma$. In the region along the jet the signal of small waves can be clearly distinguished from the background noise.

632 vertical group speed (vertical particle motion). Since λ_z is large, and energy goes downward
 633 the waves can trigger motion in the lower layer. Here, due to the strong stratification,
 634 vertical motion is suppressed and the particles move horizontally (horizontal group velocity
 635 and vertical phase speed), implying a frequency close to f , a very small vertical wavelength
 636 and important dissipation. Therefore, because the wave packets cannot move deep into the
 637 stratified layer, it is no surprise that we cannot see much wave activity in the stratified layers.

638
 639 In Figure 14(b) the red contour lines indicate the values of the local Rossby number exceeding
 640 the threshold $Ro > 1$. An increment of the local Rossby number above 1, defined
 641 as

$$Ro_L = \frac{U}{fL}, \tag{20}$$

642 where $U = \sqrt{u^2 + v^2}$ is the local shear, $f = 2\Omega$ is the Coriolis parameter and $L = 1/5(b - a)$
 643 is the typical jet width, can indicate a local imbalance. While at this fluid height only two
 644 wave packets are visible at $t \simeq 400$ s and $t \simeq 700$ s, a different behaviour is observed in
 645 the uppermost layer ($z = 94$ mm) where the wave trains appear to be emitted continuously
 646 from the jet stream where the Rossby number has typical values of 2 (plot of Ro not shown
 647 here). Despite this difference, in both cases a clear spatial-temporal correlation between the
 648 highest values of the local Rossby number and the waves emission is found. This suggests

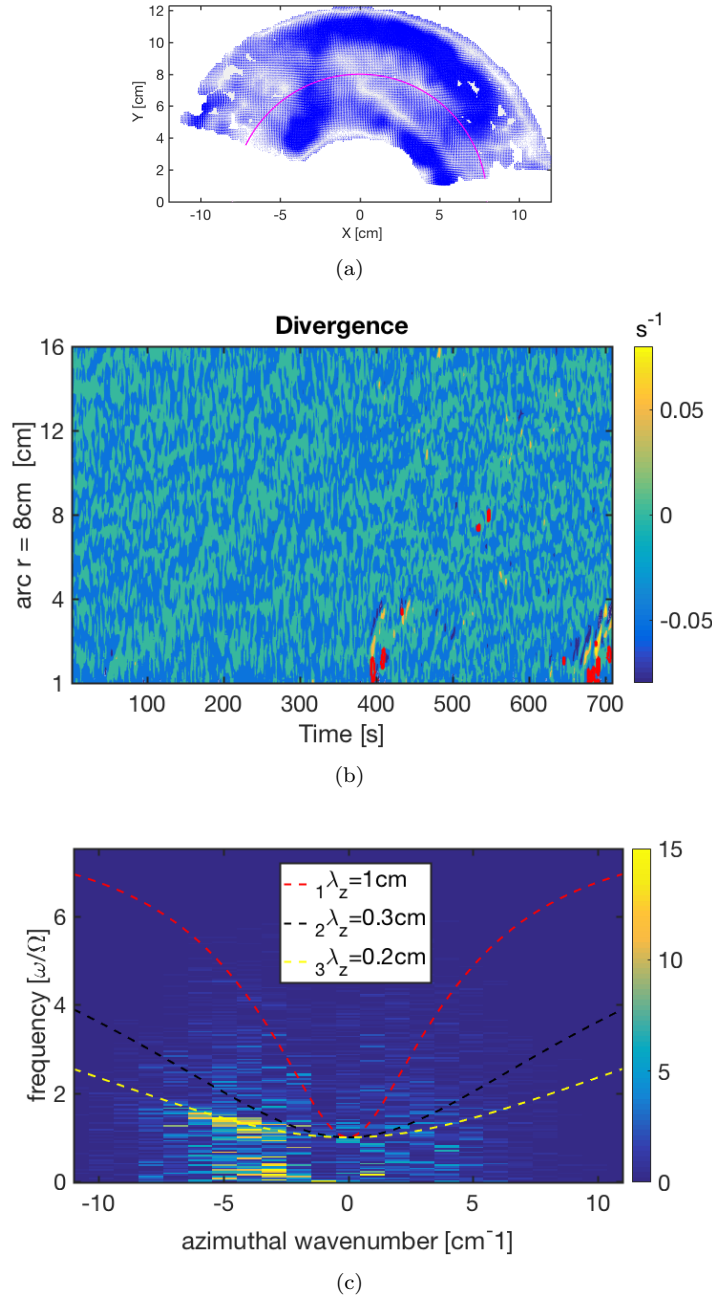


Figure 14. (a) circle of constant radius $r = 8$ cm along which the data are taken for the plots (b) and (c). (b) Hovmöller plot of the divergence at $z = 75$ mm, the red contour lines are $Ro > 1$. (c) 2D fft of the divergence space-time data plotted in (b). The dashed coloured lines show the dispersion relation for gravity waves (1) considering a horizontal wavenumber $K_H = \sqrt{k^2 + l^2}$ ranged from -12 cm^{-1} to 12 cm^{-1} and vertical wavenumbers $n_1 = 2\pi/1\lambda_z = 6.3$ cm^{-1} , $n_2 = 2\pi/2\lambda_z = 18.8$ cm^{-1} , and $n_3 = 2\pi/3\lambda_z = 31.4$ cm^{-1} . The dispersion curves are Doppler shifted according to (17) with $u_0 = 1$ mm s^{-1} and a horizontal wavenumber $K_H = 5$ cm^{-1}

649 spontaneous imbalance as generating mechanism, since stronger IGWs radiation is to be
 650 expected from regions of imbalance where wind speeds are strong (O’sullivan and Dunkerton
 651 1995).

652

653 A complete analysis of the generation mechanisms of the short scale waves observed in our
 654 experiment is beyond the purpose of this paper. Nevertheless, some possible wave excitation
 655 mechanisms can be investigated with the available data. One is excitation due to convection,

656 and this can be excluded since the gravity waves have not been found in our experimental setup
 657 without rotation, i.e., without the baroclinic jet. Kelvin-Helmholtz and Hölmboë instability
 658 are also mechanisms that might be responsible for small-scale waves emission. To distinguish
 659 between these two instabilities, it is necessary to know the interface thickness in shear and
 660 density. When their ratio exceeds a threshold usually considered being equal to 2, or more
 661 in general in the condition where a thick shear layer and a sharp density interface develop,
 662 Hölmboë instability can occur. A detailed analysis of these two instabilities and on other
 663 small-scale waves possible generating mechanism can be found in the paper by Scolan *et al.*
 664 (2014). Because we do not know precisely the thickness of the interfaces, we can not distinguish
 665 between these two shear instabilities. Nevertheless, we can estimate the Richardson number

$$666 \quad Ri = \frac{N^2}{(du/dz)^2}, \quad (21)$$

666 where $u(z)$ is the horizontal velocity profile, and check whether the Miles criterion for stratified
 667 shear instability is satisfied. $Ri \geq 1/4$ is the sufficient condition for the stability of a sheared,
 668 stratified flow. We can use the values of the azimuthal velocity at $z = 94$ mm and $z = 75$ mm
 669 to estimate the vertical shear and the values of N estimated previously to calculate the
 670 Richardson number at these two locations. Note that this is only a crude estimation because
 671 we have only two measures of the velocity. If we use the value of N ($\simeq 0.1$ rad/s) that permits
 672 the existence of IGWs, the Richardson number at $z = 94$ mm is $Ri^{94} = 0.39$ which is above
 673 but close to $1/4$, i.e. just around the limit to rule out shear instabilities. The paradox being
 674 of course that if we imagine a higher estimated value of N (say $N = 0.2$ rad/s for instance),
 675 then we cannot interpret the small scales waves observed at $z = 94$ mm neither by IGWs (the
 676 dispersion relation will not be fulfilled) nor by shear instability as the Richardson number will
 677 strongly differ from $1/4$. Fortunately, at $z = 75$ mm, the situation is different as the dispersion
 678 relation for IGWs is clearly validated and moreover, using the value $N_{75} = 3.8$ rad/s, the
 679 Richardson number at this location is $Ri^{75} = 564$. This value, being strongly larger than
 680 $1/4$, confirms a stably stratified shear flow that rules out any Kelvin-Helmholtz or Hölmboë
 681 instability. Moreover, the position of small-scale waves with respect to the baroclinic jet and
 682 their occurrence related to an enhanced value of the local Rossby number (Figure 14(b))
 683 does point to spontaneous imbalance as generating mechanism. However, even if we are fully
 684 confident for the results at $z = 75$ mm, our analysis is rather coarse compared to the one done
 685 for the two-layer case by Scolan *et al.* (2014) and further investigations are needed to confirm
 686 the generation mechanism of the small-scale waves in the continuously stratified case.

687

688 Finally, we want to mention that optical deformation of the free surface due to capillary
 689 waves would have a much larger phase speed than the waves we observed. We conclude that
 690 capillary waves are not responsible for the small-scale structures at the free surface.

691 **5. Conclusions**

692 The differentially heated rotating annulus is a classical laboratory experiment to study large-
693 scale baroclinic waves and their interactions. Here, in contrast, we focused on the existence and
694 interaction of different wave types in a modified version of the classical experiment: instead of
695 stratification due to differentially heating the lateral walls alone we added salt stratification
696 in the axial direction and hence considered a thermohaline version of the experiment. The
697 novel feature in this configuration is the occurrence of thin convectively mixed layers at the
698 top and the bottom where baroclinic instability can take place and a thicker stable stratified,
699 dynamically less active layer in between.

700 For this configuration, we experimentally observed two different baroclinic waves with az-
701 imuthal wavenumber 3 for the top and 4 for the bottom layer. The former was in a steady
702 state with a slow drift rate exciting higher harmonics by self-interaction. The latter showed
703 amplitude vacillations and a fast drift. The vacillations result from the interaction between
704 two $m = 4$ waves with different phase speeds as was described earlier by Buzyna *et al.* (1989)
705 for a classical annulus experiment. Though nonlinear triadic interaction between the waves
706 in the individual layers can clearly be seen in the spectra it is not clear yet whether the
707 baroclinic waves in the surface and bottom layers are coupled. What is striking is the close
708 correspondence of some prominent peaks in the spectra: the wave peak in the top layer is
709 very close to the difference of the frequencies of the two dominant wavenumber 4 modes in
710 the bottom layer implying a ‘frequency triad’ between top and bottom layer waves. Moreover,
711 the two harmonic frequencies of the upper layer wave nearly correspond to the frequency of
712 the two wavenumber 4 waves in the bottom layer.

713 Besides the large-scale baroclinic waves, we further observe an inertial Kelvin type global
714 mode and a higher frequency surface wave of Poincaré type. The inertial Kelvin mode shows
715 similarity with a shallow water boundary trapped Kelvin wave, has an azimuthal wavenumber
716 1 but has the frequency of the tank’s rotation and not f . It is hence not a shallow water mode
717 but an inertial wave Kelvin mode with a certain vertical structure. Unfortunately, since we
718 did not measure simultaneously at different vertical levels we do not know the vertical wave
719 number. We just know that the inertial Kelvin mode is strongest in the non-convective zone
720 and the bottom layer. The mode is very likely mechanically driven by a slight deviation of
721 the rotation axis from vertical.

722 The origin of the Poincaré type modes with frequencies larger than f is not yet clear.
723 They might also be triggered mechanically by a very weak sloshing of the tank. A theoretical
724 treatment of those modes (as done by Mougél *et al.* (2015) for the homogeneous case) is
725 hampered by the nonlinear vertical density profile. For a thorough analysis, effects at the
726 internal interfaces have to be considered in addition to the surface wave modes. Such a study
727 is postponed to the future when more data, in particular in the high frequency range and
728 from vertical cross sections are available.

729 A long standing problem is whether in differentially rotating annulus experiments instabil-
730 ities of baroclinic fronts and in particular spontaneous imbalance of the frontal flow can be
731 observed. Short interfacial wave patterns have been observed in experiments by Lovegrove
732 *et al.* (2000) and Williams *et al.* (2005), even though the source for these patterns is not fully
733 clear yet (Flór *et al.* 2011). In contrast to the global modes described above such short-wave
734 inertia-gravity waves are hard to be found in the wave spectra since they typically occur spo-
735 radically and are spatially localized since they are tightly connected to the baroclinic front.
736 Although spontaneous imbalance has been documented from a number of numerical simula-
737 tions also for the annulus configuration (Borchert *et al.* (2014) and Hien *et al.* (2018)) for
738 which Reynolds number like in the experiment was rather small ($Re \simeq 100$) it has never
739 been experimentally observed for the continuously stratified annulus for which in general the
740 Rossby numbers are rather small and the flow is in a nearly balanced state. In our experiments

741 the top layer shows wave packets in the horizontal divergence field travelling mainly with the
 742 frontal mean flow and hence much faster than the drift speed of the baroclinic waves. These
 743 structures are not unlike the wave trains described by O’sullivan and Dunkerton (1995). We
 744 have shown that their signal is above the noise level, their frequencies are in the inertia-gravity
 745 wave range and that the frequency-wavenumber plot roughly follows one branch of the disper-
 746 sion curves. We speculate that compared to the classical “Hide” experiment its thermohaline
 747 version is more suitable to find such waves. However for sound evidence, whether the waves in
 748 the mixed baroclinically unstable layer are generated by shear instability or spontaneously, we
 749 need data on the temperature related N . Then we can also determine N/f in the baroclinic
 750 layers which is larger than one for the atmosphere but smaller than one for the “Hide” exper-
 751 iment. For the classical annulus, inertia is dominant and the baroclinic fronts do occur over
 752 the full depth of the tank and not just in thin layers. The latter might be more favourable to
 753 generate frontal waves. Moreover, we want to mention that in contrast to the classical setup,
 754 no numerical simulation is available for the barostrat case.

755 We have experimentally demonstrated that the thermohaline version of the differentially
 756 heated rotating annulus is not only a testbed to study large-scale wave interactions but is
 757 also a setup suitable to study interactions of different wave types. The natural layer formation
 758 offers the possibility to investigate wave resonance but also wave propagation between the
 759 different layers. The dynamically passive layer in the annulus center might be seen as a model
 760 for the stratosphere comprised between baroclinically unstable tropospheres as was proposed
 761 by Vincze *et al.* (2016).

762 6. Acknowledgments

763 This work was supported by the Spontaneous Imbalance project (HA 2932/8-1) that is part
 764 of the research group Multiscale Dynamics of Gravity Waves funded by DFG (FOR1898).
 765 This study was initiated by the European High-performance Infrastructures in Turbulence
 766 (EuHIT) program and PLG and UH also thank the CNRS LIA 1092-ISTROF for its financial
 767 support. M.V. is grateful for the support by the Hungarian National Research, Development
 768 and Innovation Office (NKFIH) under Grant Number FK125024. The authors thank Ludwig
 769 Stapelfeld, Robin Stöbel, Vilko Ruoff for technical support, Joel Sommeria for the support
 770 with the UVmat software and Chantal Staquet for the helpful discussions. Moreover we thank
 771 the Spontaneous Imbalance group of MS-GWaves, (Ulrich Achatz, Steffen Hien, Joran Rol-
 772 land, Lena Schoon, Christoph Zülicke, Illia Horenko, Olga Kaiser) for support and fruitful
 773 discussions. Finally we thank the two anonymous referees for their comments that helped to
 774 improve the clarity of the paper.

775 Appendix A: PIV error

776 An estimation of the error coming directly from the PIV software used to get the ve-
 777 locities field from the images (UVmat) is given by two quantities directly calculated
 778 by the software, namely the *rms* difference between the CIV (Correlation Image Ve-
 779 locimetry) and the smoothed velocity field, and secondly the number of vectors excluded
 780 because attributed to false vectors (<http://servforge.legi.grenoble-inp.fr/projects/soft-uvmat/wiki/Tutorial/CorrelationImageVelocimetryOptimisation>). For our data the values
 781 are $rms = 0.5 - 0.6$ pixels for a typical displacement of 5 pixels. This gives an estimation
 782 of the PIV error 10% – 12%. The percentile of excluded vectors is less than 1.5%, so most
 783 vectors are preserved.
 784

786 The a posteriori quantification of the error on the PIV data we propose here is done by
 787 taking two consecutive PIV images ($\Delta T = 0.03$ s) and subtracting the velocity fields. Because
 788 our flow is rather slow, one can expect that the fields do not differ too much and they are
 789 completely uncorrelated from one to the other because to compute the PIV we use two different
 790 sets of images. From this we can calculate the relative error for the velocity components as

$$err = \frac{V_1 - V_2}{V_1 + V_2} \quad (\text{A.1})$$

791 Repeating this procedure for the entire time serie, we can estimate the mean error associated
 792 to the PIV data analysis for the U and V components of the velocity. The calculated mean
 793 error is less than 15% across the whole domain, comparable with the error estimation
 794 obtained from UVmat software.

795

796 The signal-to-noise ratio, used to compare the level of the IGWs signal to the level of the
 797 background noise, is calculated as

$$SNR = \frac{\mu}{\sigma} \quad (\text{A.2})$$

798 where σ is the square root of the mean variances of the background noise, i.e., calculated in
 799 an area where no IGWs signal is visible in the divergence field and μ is the locally (over a
 800 square running filter of dimensions 10×10 mm) averaged divergence field.

801 References

- 802 Boehrer, B., Double-diffusive convection in lakes. In *Encyclopedia of Lakes and Reservoirs*, pp. 223–224, 2012
 803 (Dordrecht: Springer).
- 804 Borchert, S., Achatz, U. and Fruman, M.D., Gravity wave emission in an atmosphere-like configuration of the
 805 differentially heated rotating annulus experiment. *Journal of Fluid Mechanics*, 2014, **758**, 287–311.
- 806 Buzyna, G., Pfeffer, R.L. and Kung, R., Kinematic properties of wave amplitude vacillation in a thermally
 807 driven rotating fluid. *Journal of the Atmospheric Sciences*, 1989, **46**, 2716–2730.
- 808 Chen, C., Briggs, D. and Wirtz, R., Stability of thermal convection in a salinity gradient due to lateral heating.
 809 *International Journal of Heat and Mass Transfer*, 1971, **14**, 57IN163–62IN365.
- 810 Flór, J.B., Scolan, H. and Gula, J., Frontal instabilities and waves in a differentially rotating fluid. *Journal of*
 811 *Fluid Mechanics*, 2011, **685**, 532–542.
- 812 Fritts, D.C. and Nastrom, G.D., Sources of mesoscale variability of gravity waves. Part II: Frontal, convective,
 813 and jet stream excitation. *Journal of the Atmospheric Sciences*, 1992, **49**, 111–127.
- 814 Früh, W.G. and Read, P., Wave interactions and the transition to chaos of baroclinic waves in a thermally driven
 815 rotating annulus. *Philosophical Transactions of the Royal Society of London A: Mathematical, Physical and*
 816 *Engineering Sciences*, 1997, **355**, 101–153.
- 817 Früh, W.G., Amplitude Vacillation in Baroclinic Flows. *Modeling Atmospheric and Oceanic Flows: Insights*
 818 *from Laboratory Experiments and Numerical Simulations*, 2014, **205**.
- 819 Fultz, D., Long, R.R., Owens, G.V., Bohan, W., Kaylor, R. and Weil, J., Studies of thermal convection in a
 820 rotating cylinder with some implications for large-scale atmospheric motions. *Meteorological Monographs*,
 821 1959, **21**, 1–104.
- 822 Guimbard, D., Le Dizès, S., Le Bars, M., Le Gal, P. and Leblanc, S., Elliptic instability of a stratified fluid in
 823 a rotating cylinder. *Journal of Fluid Mechanics*, 2010, **660**, 240–257.
- 824 Gula, J., Zeitlin, V. and Plougonven, R., Instabilities of two-layer shallow-water flows with vertical shear in
 825 the rotating annulus. *Journal of Fluid Mechanics*, 2009, **638**, 27–47.
- 826 Harlander, U., von Larcher, T., Wang, Y. and Egbers, C., PIV-and LDV-measurements of baroclinic wave
 827 interactions in a thermally driven rotating annulus. *Experiments in fluids*, 2011, **51**, 37–49.
- 828 Hide, R. and Mason, P., Sloping convection in a rotating fluid. *Advances in Physics*, 1975, **24**, 47–100.
- 829 Hide, R., Mason, P. and Plumb, R., Thermal convection in a rotating fluid subject to a horizontal temperature
 830 gradient: spatial and temporal characteristics of fully developed baroclinic waves. *Journal of the Atmospheric*
 831 *Sciences*, 1977, **34**, 930–950.
- 832 Hide, R., An experimental study of thermal convection in a rotating liquid. *Philosophical Transactions of the*
 833 *Royal Society of London A: Mathematical, Physical and Engineering Sciences*, 1958, **250**, 441–478.
- 834 Hien, S., Rolland, J., Borchert, S., Schoon, L., Zülicke, C. and Achatz, U., Spontaneous inertia-gravity wave
 835 emission in the differentially heated rotating annulus experiment. *Journal of Fluid Mechanics*, 2018, **838**,
 836 5–41.

- 837 Hignett, P., Characteristics of amplitude vacillation in a differentially heated rotating fluid annulus. *Geophysical*
838 *& Astrophysical Fluid Dynamics*, 1985, **31**, 247–281.
- 839 Jacoby, T., Read, P., Williams, P.D. and Young, R., Generation of inertia–gravity waves in the rotating thermal
840 annulus by a localised boundary layer instability. *Geophysical & Astrophysical Fluid Dynamics*, 2011, **105**,
841 161–181.
- 842 Lacaze, L., Le Gal, P. and Le Dizès, S., Elliptical instability in a rotating spheroid. *Journal of Fluid Mechanics*,
843 2004, **505**, 1–22.
- 844 Lagrange, R., Meunier, P., Nadal, F. and Eloy, C., Precessional instability of a fluid cylinder. *Journal of Fluid*
845 *Mechanics*, 2011, **666**, 104–145.
- 846 Lindzen, R.S., Farrell, B. and Jacqmin, D., Vacillations due to wave interference: applications to the atmosphere
847 and to annulus experiments. *Journal of the Atmospheric Sciences*, 1982, **39**, 14–23.
- 848 Lorenz, E.N., Empirical orthogonal functions and statistical weather prediction. *Scientific Report No. 1. De-*
849 *partment of Meteorology, MIT*, 1956.
- 850 Lovegrove, A., Read, P. and Richards, C., Generation of inertia-gravity waves in a baroclinically unstable fluid.
851 *Quarterly Journal of the Royal Meteorological Society*, 2000, **126**, 3233–3254.
- 852 Marple, L., Computing the discrete-time "analytic" signal via FFT. *IEEE Transactions on signal processing*,
853 1999, **47**, 2600–2603.
- 854 Medrano, M., Garaud, P. and Stellmach, S., Double-diffusive mixing in stellar interiors in the presence of
855 horizontal gradients. *The Astrophysical Journal Letters*, 2014, **792**, L30.
- 856 Mougel, J., Fabre, D. and Lacaze, L., Waves in Newton's bucket. *Journal of Fluid Mechanics*, 2015, **783**,
857 211–250.
- 858 Navarra, A. and Simoncini, V., *A guide to empirical orthogonal functions for climate data analysis*, 2010
859 (Springer Science & Business Media).
- 860 Ohlsen, D.R. and Hart, J.E., Nonlinear interference vacillation. *Geophysical & Astrophysical Fluid Dynamics*,
861 1989, **45**, 213–235.
- 862 Oster, G. and Yamamoto, M., Density Gradient Techniques.. *Chemical Reviews*, 1963, **63**, 257–268.
- 863 O'sullivan, D. and Dunkerton, T.J., Generation of inertia–gravity waves in a simulated life cycle of baroclinic
864 instability. *Journal of the Atmospheric Sciences*, 1995, **52**, 3695–3716.
- 865 Pfeiffer, R.L., Ahlquist, J., Kung, R., Chang, Y. and Li, G., A study of baroclinic wave behavior over bottom
866 topography using complex principal component analysis of experimental data. *Journal of the Atmospheric*
867 *Sciences*, 1990, **47**, 67–81.
- 868 Randriamampianina, A. and del Arco, E.C., Inertia–gravity waves in a liquid-filled, differentially heated, ro-
869 tating annulus. *Journal of Fluid Mechanics*, 2015, **782**, 144–177.
- 870 Randriamampianina, A., Früh, W.G., Read, P.L. and Maubert, P., Direct numerical simulations of bifurcations
871 in an air-filled rotating baroclinic annulus. *Journal of Fluid Mechanics*, 2006, **561**, 359–389.
- 872 Scolan, H., Verzicco, R. and Flór, J.B., Frontal Instabilities at Density–Shear Interfaces in Rotating Two-
873 Layer Stratified Fluids. *Modeling Atmospheric and Oceanic Flows: Insights from Laboratory Experiments*
874 *and Numerical Simulations*, 2014, **205**.
- 875 Shibley, N.C., Timmermans, M.L., Carpenter, J.R. and Toole, J.M., Spatial variability of the Arctic Ocean's
876 double-diffusive staircase. *Journal of Geophysical Research: Oceans*, 2017, **122**, 980–994.
- 877 Thomson, R.E. and Emery, W.J., *Data Analysis Methods in Physical Oceanography*, 2001 (Elsevier).
- 878 Triana, S., Zimmerman, D. and Lathrop, D., Precessional states in a laboratory model of the Earth's core.
879 *Journal of Geophysical Research: Solid Earth*, 2012, **117**.B4.
- 880 Uccellini, L.W. and Koch, S.E., The synoptic setting and possible energy sources for mesoscale wave distur-
881 bances. *Monthly weather review*, 1987, **115**, 721–729.
- 882 Vallis, G.K., *Atmospheric and oceanic fluid dynamics: fundamentals and large-scale circulation*, 2006 (Cam-
883 bridge University Press).
- 884 Vincze, M., Harlander, U., von Larcher, T. and Egbers, C., An experimental study of regime transitions in a
885 differentially heated baroclinic annulus with flat and sloping bottom topographies. *Nonlinear Processes in*
886 *Geophysics*, 2014, **21**, 237–250.
- 887 Vincze, M., Borchert, S., Achatz, U., von Larcher, T., Baumann, M., Liersch, C., Remmler, S., Beck, T.,
888 Alexandrov, K.D., Egbers, C. *et al.*, Benchmarking in a rotating annulus: a comparative experimental and
889 numerical study of baroclinic wave dynamics. *Meteorologische Zeitschrift*, 2015, pp. 611–635.
- 890 Vincze, M., Borgia, I., Harlander, U. and Le Gal, P., Double-diffusive convection and baroclinic instability
891 in a differentially heated and initially stratified rotating system: the barostrat instability. *Fluid Dynamics*
892 *Research*, 2016, **48**, 061414.
- 893 Viúdez, Á. and Dritschel, D.G., Spontaneous generation of inertia–gravity wave packets by balanced geophysical
894 flows. *Journal of Fluid Mechanics*, 2006, **553**, 107–117.
- 895 Von Larcher, T. and Egbers, C., Experiments on transitions of baroclinic waves in a differentially heated
896 rotating annulus. *Nonlinear Processes in Geophysics*, 2005, **12**, 1033–1041.
- 897 Williams, P.D., Haine, T.W. and Read, P.L., On the generation mechanisms of short-scale unbalanced modes
898 in rotating two-layer flows with vertical shear. *Journal of Fluid Mechanics*, 2005, **528**, 1–22.